Breaking Solitary Waves and Breaking Wave Forces on a Vertically Mounted Slender Cylinder over an Impermeable Sloping Seabed

Mayilvahanan Alagan Chella[1]*, Hans Bihs[1], Dag Myrhaug[2], Michael Muskulus[1]
[1]Department of Civil and Environmental Engineering
[2]Department of Marine Technology
Norwegian University of Science and Technology (NTNU), 7491 Trondheim, Norway

Journal of Ocean Engineering and Marine Energy, 2017, **3** , pp. 1-19.

Abstract

In the present study, breaking solitary waves over a sloping seabed and breaking wave forces on a vertically mounted cylinder are simulated with the three-dimensional CFD model REEF3D. The numerical model uses the Reynolds-Averaged Navier-Stokes (RANS) equations together with the level set method (LSM) for the free surface and the $k - \omega$ for the turbulence. The numerical model is validated for simulating breaking solitary waves and breaking wave forces against the experimentally measured free surface profiles and vertical and horizontal velocities by Mo et al. (2013) and the experimentally measured free surface elevation and breaking wave force by Chakrabarti et al. (1997). The main purpose of the paper is to examine the effects of the breaking characteristics, the geometric properties, the relative cylinder positions and the incident wave heights on the breaking wave force characteristics. A total of 21 simulations are performed to investigate the characteristics and the geometric properties of solitary waves breaking over a slope and the associated breaking wave forces on a cylinder. First, the characteristics and geometric properties of breaking solitary waves are investigated with two-dimensional simulations. Further, the study explores the effect of the relative distance between the breaking point and the cylinder on breaking wave forces. Finally, the study examines breaking solitary wave forces for different incident waves. This also includes the analysis of breaking wave force characteristics such as the impact duration and rise time, the peak force, the average slamming coefficient, and the force impulse. The results of the numerical simulations show that the relative distance between the cylinder and the breaking point plays an important role in obtaining the maximum force. In addition, the numerical model is capable of representing the most important physical flow features related to the breaking solitary waves and the interaction with the vertical slender cylinder.

---

*Corresponding author, mayilvahanan.a.chella@ntnu.no

Keywords:

Solitary waves, wave structure interaction, breaking waves, geometric properties, breaking characteristics, breaking wave forces

1 Introduction

The wave transformation process in shallow waters is strongly influenced by seabed interaction. As a result, the wave height increases with a steeper wave front, gains forward momentum and the wave front becomes nearly vertical at the breaking point. When the vertical wave front hits the surface of a structure, a sudden drop in the forward momentum leads to an impact force of large magnitude with short duration. The wave impact characteristics are determined by the breaker type and breaker point. The breaker types can be grouped into four types: spilling, plunging, surging and collapsing, and are determined by the incident wave characteristics and beach slope (Galvin, 1968). The knowledge of the wave impact loads from the steep and breaking waves is important for an understanding of the global load characteristics on structures deployed in shallow waters; e.g. substructures for offshore wind turbines (Alagan Chella et al., 2012).

The solitary wave theory is appropriate for describing the propagation of long-period oscillatory waves in shallow waters. Moreover, the propagation and interaction of tsunami waves with coastal structures can be well represented with an appropriate solitary wave theory. Solitary breaking waves exert huge hydrodynamic loads on support structures in shallow waters. Goring (1978) performed numerical and experimental investigations on the wave propagation of long waves in shallow waters. Different theoretical approaches such as linear and nonlinear dispersive and linear and nonlinear nondispersive wave theories were considered. The author also investigated the transmission and reflection properties of solitary and cnoidal waves, which are relevant for the propagation of tsunami waves from deep waters to shallow coastal waters. Losada et al. (1989) examined the propagation of non-breaking solitary waves over a step. The various aspects of solitary wave characteristics were investigated. The shoaling and the breaking characteristics of solitary waves over plane slopes have been extensively studied by Munk (1949); Ippen and Kulin (1954); Miles (1980); Grilli et al. (1995, 1997); Camfield and Street (1979).

An analytical model for predicting impact pressures on vertical walls due to breaking waves was proposed by Cooker and Peregrine (1990, 1995) based on the pressure-impulse theory. The peak pressure distribution and the kinematics during the impact process were investigated for liquid-solid and liquid-liquid impact problems . It was found that the wave pressure impulse field is strongly influenced by the local wave characteristics during the impact. More detailed discussion on wave impact on walls can be found in Kortenhaus et al. (1999), and Peregrine (2003). Cuomo et al. (2010, 2011) investigated wave impact loads from breaking waves on vertical walls and caisson breakwaters experimentally and analytically. Based on the analysis, the authors proposed a set of new formulae for estimating both horizontal quasi-static and impact forces and overturning moments on vertical face coastal structures. The

---

Postprint, published in Journal of Ocean Engineering and Marine Energy, doi: http://dx.doi.org/10.1007/s40722-016-0055-5

estimated wave forces were in good agreement with experimental data and the predicted forces with the pressure-impulse theory (Cooker and Peregrine, 1990, 1995). Further, Cuomo et al. (2007) examined the characteristics of wave loads on offshore jetties experimentally. The force mechanism of impulsive loading process was studied with the wavelet analysis. The authors also proposed dimensionless equations to estimate wave forces on deck and beam elements.

According to Goda et al. (1966), the total wave force on a vertical pile due to breaking waves is composed of two parts. The first part is associated with a fluid force which can be represented well by the Morison equation. The other part is associated with the wave impact force arising from the complex interaction of fluid velocities and accelerations with the structure. The hydrodynamics related to the wave impact force due to breaking waves are extremely complicated. The shape of the water surface at the instant of the wave impact plays a significant role in estimating the impact force as shown in Fig. 1 (b). In the case of a nearly breaking wave in shallow water, the maximum particle velocity occurs at the crest, thus the force contribution from the crest is larger than the contribution from the rest of the wave. Therefore, the mechanism of the wave impact force mainly depends on the shape of the wave front and the wave celerity at breaking.

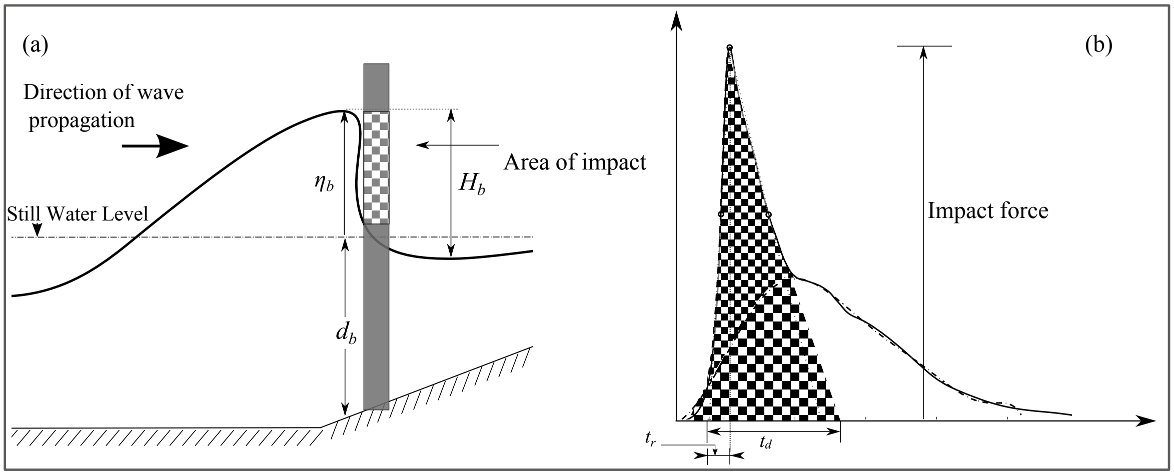

Figure 1: Definition sketch for characteristics of (a) breaking waves and (b) impact force; t_d and t_r are the duration and rise time of the impact, respectively. The area of the shaded portion in (b) represents the force impulse (I_{td}).

Kjeldsen and Myrhaug (1978) raised a concern about the geometrical description of the breaker profile in deep water since the local wave steepness is inadequate to represent it. They suggested steepness and asymmetry parameters to categorize the breaker profiles: crest front steepness (ε), crest rear steepness (δ) and vertical asymmetry factor (λ) as defined in the Fig. 2. With these parameters, the geometry of the wave profile at breaking can be defined. There has been some discussion about the geometrical properties of periodic waves in shallow water, see e.g. Adeyemo (1968); Hwang (1984); Alagan Chella et al. (2015a); **?**. However, to the knowledge of the authors, a study on the geometric properties has not been carried out for solitary waves breaking over slopes.

Laboratory experiments have contributed to the knowledge about waves breaking over

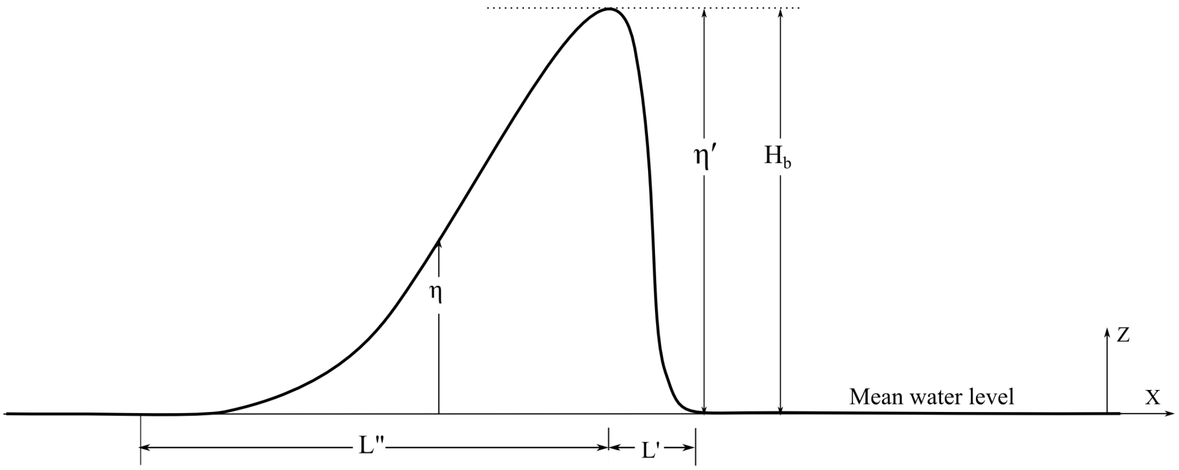

$$\varepsilon = \frac{\eta'}{L'} \qquad \delta = \frac{\eta'}{L''} \qquad \lambda = \frac{L''}{L'}$$

Figure 2: Definition sketch for crest front steepness (ε), crest rear steepness (δ) and vertical asymmetry factor (λ) following Kjeldsen and Myrhaug (1978)

beaches and the associated wave impact forces on structures; e.g. breaking waves on slopes by Adeyemo (1968); Stive and Wind (1982); Ting and Kirby (1994), and breaking wave forces by Goda et al. (1966); Sawaragi and Nochino (1984); Chaplin et al. (1992); Wienke and Oumeraci (2005); Arntsen et al. (2011). The application of the theoretical models (e.g. Wienke and Oumeraci (2005); Sawaragi and Nochino (1984)) for determining breaking wave forces is confined to the use of force and slamming coefficients. Since these coefficients are mostly obtained from physical experiments, they are subjected to the specific laboratory conditions.

The theoretical breaking criterion in deep water is always related to the physical properties of the highest steady wave, which limits the wave growth. Whereas shallow water waves deform as they propagate into decreasing water depth, the seabed friction is included as an additional effect in defining the breaking criterion in shallow water. Computational fluid dynamics (CFD) models based on the Navier-Stokes equations are capable of describing the wave transformation process including wave breaking and their non-linear interaction with structures (Lemos, 1992). CFD models can describe the breaking process without defining an empirical breaking criterion. In addition, the non-linear wave impact forces can be obtained without determining the force and slamming coefficients and curling factors . Lemos (1992) proposed a numerical model for simulating breaking waves in shallow waters based on the RANS equations, the $k - \epsilon$ model and the volume of fluid (VOF) method.

Many numerical studies have been carried out to model breaking waves in shallow waters (e.g. Lin and Liu (1998); Zhao et al. (2004); Hieu et al. (2004); Jacobsen et al. (2012); Xie (2013); Alagan Chella et al. (2015a); **?**) and associated breaking wave forces (e.g. Mo et al. (2013); Xiao and Huang (2014); Choi et al. (2015)). It is challenging to model the interaction between breaking waves and structures in the breaking zone. More recently, Mo et al. (2013) performed both experimental and numerical investigations on breaking solitary waves and its interaction with a slender cylinder over a slope. The free surface elevation and velocity at different locations were measured using PIV (Particle Image Velocimetry). They modelled the three-dimensional (3D) wave-structure interaction numerically with the filtered Navier-Stokes equations together with the Large Eddy Simulations (LES) model. Xiao and Huang (2014) modelled breaking solitary waves and breaking wave forces on a cylindrical pile using the Reynolds-Averaged Navier-Stokes (RANS) equations, the $k-\epsilon$ model and the VOF method. They studied solitary wave run-up, breaking on a slope and the breaking wave force on a vertical pile at different locations. Although the aforementioned studies reported many interesting results, little work has been carried out to study the relationship between the characteristics and geometric properties of breaking solitary waves and the resulting impact forces on structures.

The main purpose of this paper is to investigate the characteristics and geometric properties of breaking solitary waves over a slope and their interaction with a vertical circular cylinder using the two-phase flow CFD model, REEF3D (Alagan Chella et al., 2015a). The numerical model uses the RANS equations together with the level set method for the free surface and the $k-\omega$ model for turbulence. Compared to previous studies, the present study focuses on different aspects of breaking solitary wave forces on a structure in connection with the characteristics and geometric properties at breaking. The connection between the maximum total force and the cylinder location relative to the breaking point is examined.

The paper is divided into four parts. The first part deals with the validation of the numerical model. The second part examines the breaking characteristics and geometric properties of solitary waves over a sloping seabed without any structure for different incident waves with two-dimensional (2D) simulations. The third part evaluates the relative distance between the cylinder and the breaking point which significantly influences the wave impact force characteristics using 3D simulations. This has been investigated by placing a cylinder over a slope at different locations from the non-breaking zone to the post-breaking zone. In part four the effect of the incident wave height on the total force characteristics is investigated. The 3D simulations are carried out by maintaining the relative distance between the cylinder and the breaking point for different incident wave heights based on the results obtained from the second and third part. The effect of the breaking characteristics, the geometric properties, the relative cylinder positions and the incident wave heights on the the total breaking wave force characteristics are presented and discussed. Finally, conclusions are given in Part 5. Overall, the present work provides new insight into the assessment of the hydrodynamic loads on vertical cylinders and flow characteristics around them due to breaking solitary waves.

2 Numerical Model

The model proposed in this paper uses numerical approaches to enable the implementation of higher order schemes for the spatial and temporal discretization. With the higher order discretization schemes, good numerical accuracy and stability is achieved. The present numerical model has been successfully used to simulate spilling and plunging breakers over slopes (Alagan Chella et al., 2015a; **?**), waves breaking over an impermeable slope (Alagan Chella et al., 2015b), non-breaking wave forces on large cylinders (Kamath et al., 2015, 2016), and breaking wave forces on slender cylinders (Bihs et al., 2016).

A viscous incompressible two-phase flow for water and air is considered and this is described by the RANS equations. The governing equations are the continuity equation:

$$\frac{\partial U_i}{\partial x_i} = 0 \tag{1}$$

and the momentum equation:

$$\frac{\partial U_i}{\partial t} + U_j \frac{\partial U_i}{\partial x_j} = -\frac{1}{\rho}\frac{\partial P}{\partial x_i} + \frac{\partial}{\partial x_j}\left[(\nu + \nu_t)\left(\frac{\partial U_i}{\partial x_j} + \frac{\partial U_j}{\partial x_i}\right)\right] + g_i \tag{2}$$

Here U is the velocity averaged over time t, ρ is the fluid density, P is the pressure, ν is the kinematic viscosity, ν_t is the eddy viscosity, and g the gravity term.
A 5th-order Weighted Essentially Non-Oscillatory (WENO) scheme is used to discretize the non-linear convective term of the RANS equations (Jiang and Shu, 1996). Time discretization is performed by a 3rd-order total variation diminishing (TVD) Runge-Kutta scheme (Shu and Osher, 1988) which preserves numerical stability and temporal accuracy. This method involves three Euler sub-steps. Due to the lack of correlation in the pressure field (p) obtained by the solution of the Navier-Stokes equations, the pressure is modeled separately with Choriń projection method. First, an intermediate velocity (u^*) is determined by omitting the pressure term in the momentum equations. By taking the divergence of the intermediate velocity (u^*), the Poisson equation for the pressure is obtained as follows:

$$\frac{\partial}{\partial x_i}\left(\frac{1}{\rho(\phi^n)}\frac{\partial p}{\partial x_i}\right) = -\frac{1}{\Delta t}\frac{\partial U_i^*}{\partial x_i} \tag{3}$$

Then the pressure is determined by solving the Poisson equation with the BiCGStab algorithm (van der Vorst H., 1992) with Jacobi preconditioning. After solving the Poisson equation for pressure, the velocity field is updated with the projection method (Chorin, 1968) at each time step:

$$u_i^{n+1} = u_i^* - \frac{\Delta t}{\rho(\phi^n)}\frac{\partial p}{\partial x_i} \tag{4}$$

The staggered grid arrangement is implemented in the numerical model to achieve a strong pressure-velocity coupling.
Turbulence in the breaking waves is described by the $k-\omega$ model together with the standard RANS turbulence closure. An accurate representation of the interface for time-dependent free-surface flow problems is highly demanding as this involves the capturing of discontinuities in the material properties such as density and viscosity. The two-fluid interface is modelled with the level set method (Osher and Sethian, 1988) which is an Eulerian front capturing scheme. Simulations are carried out in a 3D numerical wave tank. The relaxation method is used to describe the wave generation (Larsen and Dancy, 1983; Jacobsen et al., 2012). The bed roughness considered in the numerical model is 0.0001m. The total wave forces on a structure are directly obtained by integrating the pressure and the normal component of the viscous stress tensor τ over the surface of the structure as follows:

$$F = \int_\Omega (-\mathbf{n}p + \mathbf{n}.\tau)d\Omega \tag{5}$$

where **n** is the unit normal vector to the surface, pointing into the fluid domain and Ω is the surface of the structure. More detailed information concerning the numerical model can be found in Alagan Chella et al. (2015a); **?** and Kamath et al. (2015).

3 Characteristics of breaking waves and impact force

Simulation cases	Normalized wave height, H_0/d_0	Normalized relative distance between the cylinder and the breaking point, $L_c = (H_b x_c/d_b D)$	Slope parameter, S_0	Breaker type
Case A	0.33	-12.72 -8.48 -4.24 0.000 4.24 8.48 12.72 16.96 21.20	0.236	PL
Case B 2D and 3D simulations	0.257	4.24	0.21	PL
	0.281		0.22	PL
	0.305		0.23	PL
	0.330		0.24	PL
	0.354		0.25	PL
	0.378		0.26	PL
	0.403		0.27	PL

Table 1: List of the 2D and 3D computational cases; PL: Plunging breaker.

In the present study, the breaking point is identified when most of the wave front becomes vertical and the breaker height (H_b) and water depth at breaking (d_b) are calculated as defined in Fig. 1 (a). The breaking characteristics are evaluated based on the location of the breaking point (x_b), water depth at breaking (d_b), the breaker depth index ($\gamma_b = H_b/d_b$), and the breaker height index ($\Omega_b = H_b/H_0$, where H_0 is the deep water wave height). The waves considered in the present study are plunging breaking waves as listed in Table 1. The breaker type is classified based on the slope parameter (S_0) defined by Grilli et al. (1997):

$$S_0 = 1.521\frac{m}{\sqrt{(}H_0/d_0)} \tag{6}$$

The values of slope parameter (S_0) for different breaker types:

Spilling : S_0¡0.025
Plunging: 0.025¡S_0¡0.30
Surging: 0.3¡S_0¡0.37.

A force impulse is a most common design parameter for coastal structures especially; it governs the global response of a structure (Kortenhaus et al., 1999). The force impulse (I_{td})

is described by the peak force (F_{peak}), the impact duration (t_d), and the impact rise time (t_r), and it is the area under the peak force of a force-time curve over an impact duration as defined in Fig. 1. In order to evaluate the wave impact force contribution to the total breaking wave force, the average slamming coefficient $\overline{C_s}$ proposed by Sarpkaya and Isaacson (1981) is used and it is defined as follows:

$$\overline{C_s} = \frac{F_{maxt}}{0.5\rho A_{sub} C_b^2} \tag{7}$$

where F_{maxt} is the maximum total force, D is the diameter of the cylinder, A_{sub} is the submerged projected area, and C_b is the wave celerity at the breaking point.

4 Results and discussion

4.1 Benchmark cases

4.1.1 Experimental and simulation conditions

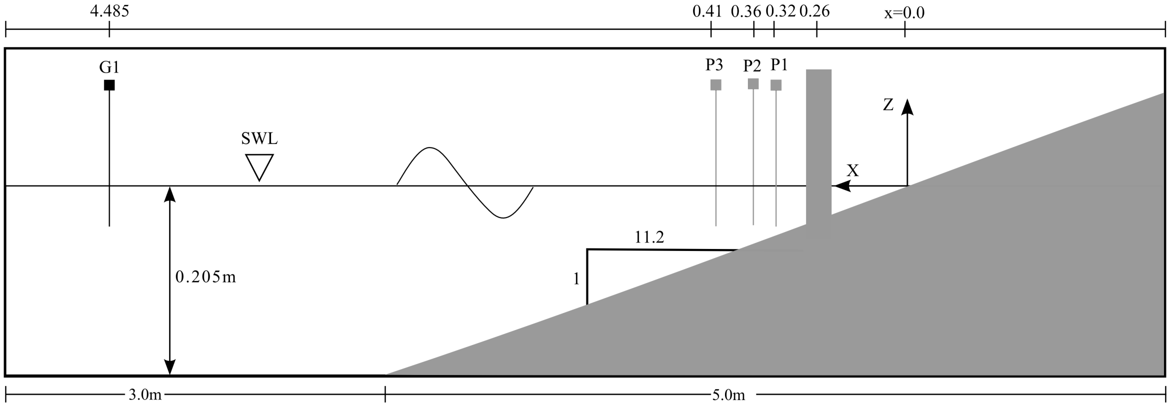

Figure 3: Computational set-up

To validate the numerical model, the simulated results are compared with the experimental results reported by Mo et al. (2013). They performed a series of laboratory experiments in a 25m long, 0.3m wide and 1.0m deep wave tank. In the present numerical study, the computation domain starts with a 3.0m long flat bed portion with a water depth of 0.205m connected to a slope of 1/11.2. The computational domain is of length L_x=12.0m, width L_y=0.01m and height $L_z = 0.50m$ for the 2D set-up (Fig. 3) and of length L_x=12.0m, width L_y=0.40m and height $L_z = 0.50m$ for the 3D set-up. At first, the 2D simulations are carried out to examine the characteristics and geometry of breaking solitary waves over a slope. The results from these 2D simulations such as the breaking point and the breaker height serve as input to the 3D simulations for case B as listed in Table 1. Since the 3D flow features are insignificant before the wave breaking, the 2D simulations are used to determine the incipient breaker characteristics and geometric properties. Further, the 3D simulations are performed with a cylinder of diameter D=0.06m placed over a slope at x=0.260m from the shoreline. The interaction of breaking waves with the cylinder and the resulting breaking wave forces are investigated. Therefore, the 3D simulations are performed to obtain the breaking wave forces and 3D flow features around the cylinder. Though the experiments were carried out in a wave tank with a flat 5.0m long bed, the numerical wave tank is reduced to 3.0m as the reduction in the flat bed part does not affect the incident wave characteristics in the flat bed region. Except for that, the coordinate system and wave parameters of the numerical simulations are the same as that of the laboratory measurements.

4.1.2 Grid dependence study

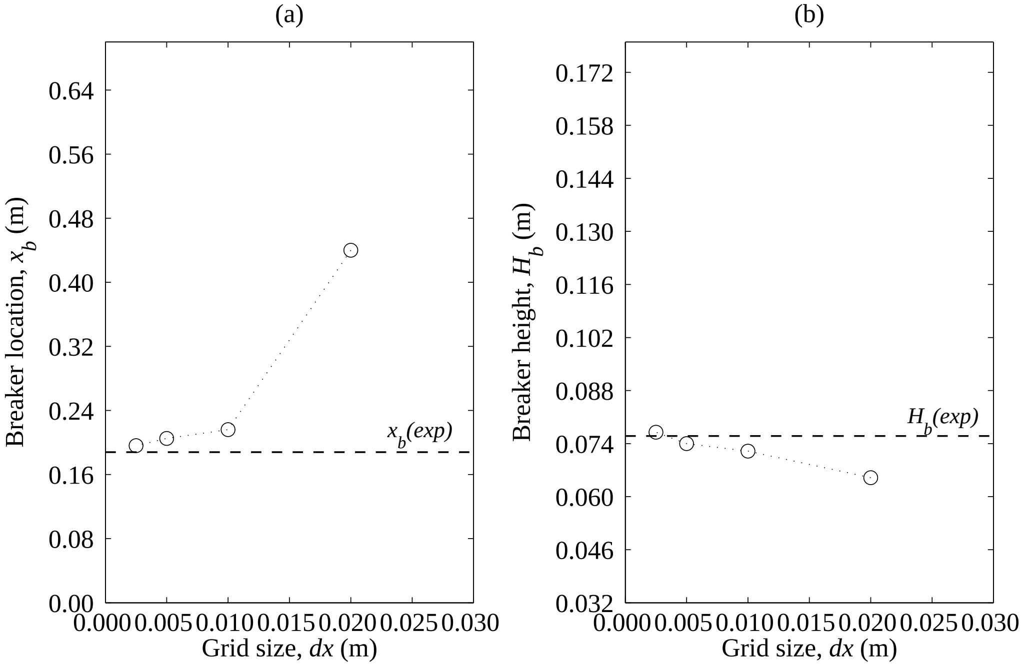

Figure 4: Grid dependency study on numerical breaking location (x_b) and breaker height (H_b); $x_b(exp)$ and $H_b(exp)$ are the experimentally measured values of x_b and H_b by Mo et al. (2013).

The sensitivity of the grid size on the computational results is investigated with four different uniform grid sizes, dx=0.0025m, 0.005m, 0.010m and 0.020m. Fig. 4 shows the breaker location (x_b) and the breaker height (H_b) for these grid sizes. In contrast to cnoidal waves on slopes (Alagan Chella et al., 2015a), the simulated waves with the coarsest grid (dx=0.020m) reach the breaking point sooner with lower H_b than that of the waves with finer grids, corresponding to dx=0.02, x_b=0.44m (Fig. 4 (a)) and H_b=0.065m (Fig. 4 (b)). The numerical results for dx=0.0025m, 0.005m and 0.010m are close to the laboratory breaking location x_b=0.188m and the breaker height H_b=0.076m as shown in Fig. 4. In addition, the 3D simulations are computationally quite expensive. Therefore, the grid size dx=0.010m is used for the following simulations with 55981 number of cells for 2D simulations and 1648400 number of cells for 3D simulations.

4.1.3 Solitary wave generation and breaking over a sloping seabed

In the wave generation zone, the free surface elevation and the kinematics are described using the third-order solitary wave theory proposed by Grimshaw (1971). The solitary wave with the normalized wave height of H_0/d_0=0.33 is generated for the constant water depth of

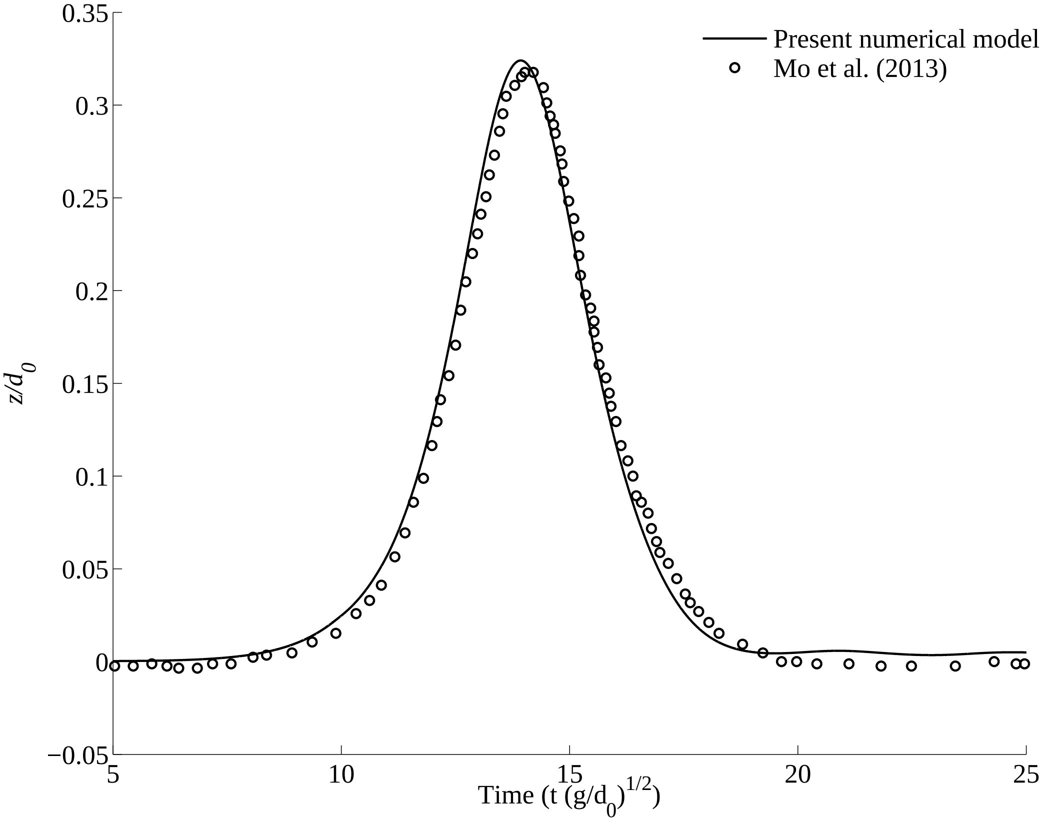

Figure 5: Comparison of numerical and experimental free surface elevation at x=4.485m, circles: experimental data by Mo et al. (2013); solid lines: present numerical results;

d_0=0.205m. The comparison of the numerical wave surface elevation at x=4.485m shows a good agreement with the experimental data by Mo et al. (2013) as presented in Fig. 5. This confirms that the laboratory waves are well represented by the numerically generated waves. Figs. 6 and 7 show the comparison of the 2D numerical wave profiles at $t\sqrt{g/d_0}$=31.35 and 31.77, respectively, and the corresponding normalized horizontal velocity profiles at x=0.32m, 0.36m and 0.41m with the experimental results. The velocity profiles at different locations are computed from the seabed up to the free surface in the numerical simulations while the laboratory profiles are measured up to a point little above the free surface in the air phase. The computed and measured horizontal component of velocity increase as the distance from the bottom increases. At the crest, the horizontal component of velocity increases with increasing wave surface elevation (Fig. 6). It is noticed that the computed velocity profiles have large gradients close to the seabed due to the boundary layer effect. However, the spatial resolution of the numerical results are not sufficiently small to account for the boundary layer effects close to the seabed; strictly it should approach zero at the bed. It was reported by Mo et al. (2013) that the boundary layer effects near the seabed was not captured well in the laboratory experiments due to the low resolution in the measurements.

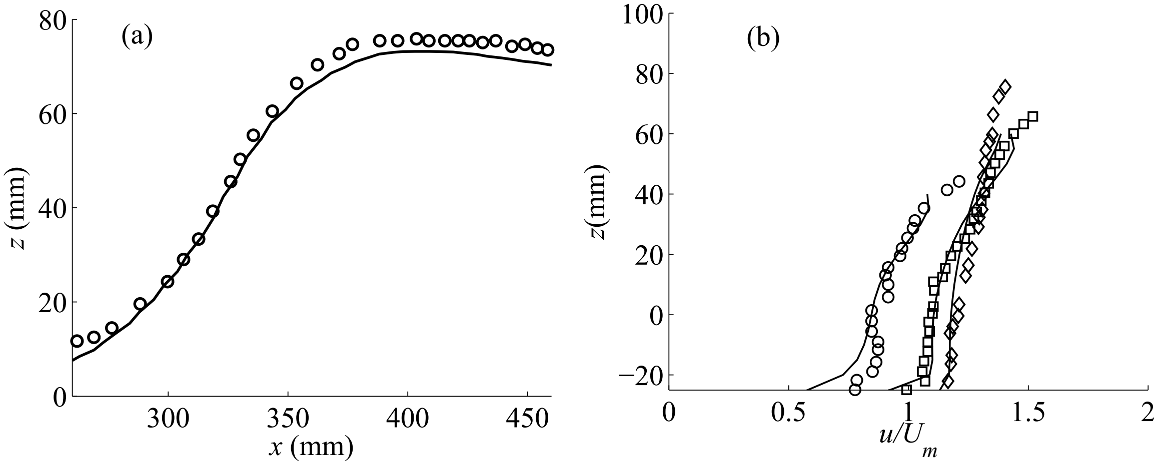

Figure 6: Comparison of numerical (solid lines) and experimental results for (a) wave surface elevation at $t\sqrt{g/d_0}$=31.35 (circles: experimental data) and (b) horizontal velocity profiles at x=0.32m (circles: experimental data), 0.36m (squares: experimental data) and 0.41m (diamonds: experimental data); U_m is the computed mean horizontal velocity and the value is 726 mm/s.

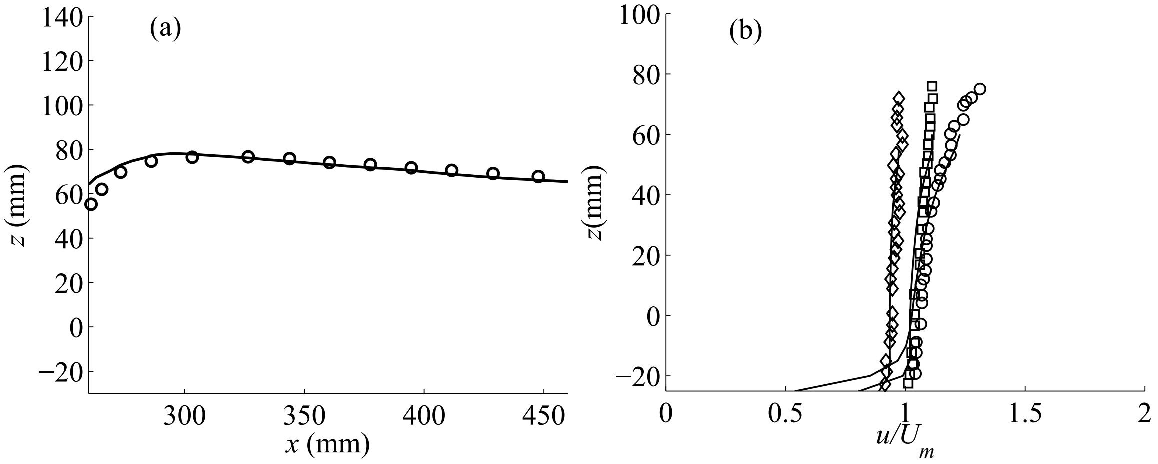

Figure 7: Comparison of numerical (solid lines) and experimental results for (a) wave surface elevation at $t\sqrt{g/d_0}$=31.77 (circles: experimental data) and (b) horizontal velocity profiles at x=0.32m (circles: experimental data), 0.36m (squares: experimental data) and 0.41m (diamonds: experimental data); U_m=768 mm/s

Fig. 8 shows the evolution of the free surface profiles of the wave approaching breaking and the comparison with the experimental data. The simulated free surface profiles are in good agreement with those measured by Mo et al. (2013). The wave front becomes steep as the wave propagates over the slope due to the shoaling and the wave front becomes vertical and breaks at x=0.216m which is very close to the laboratory breaking (x_b=0.188m). Further, the wave crest overturns with a forward ejected water jet due to high velocities at the wave

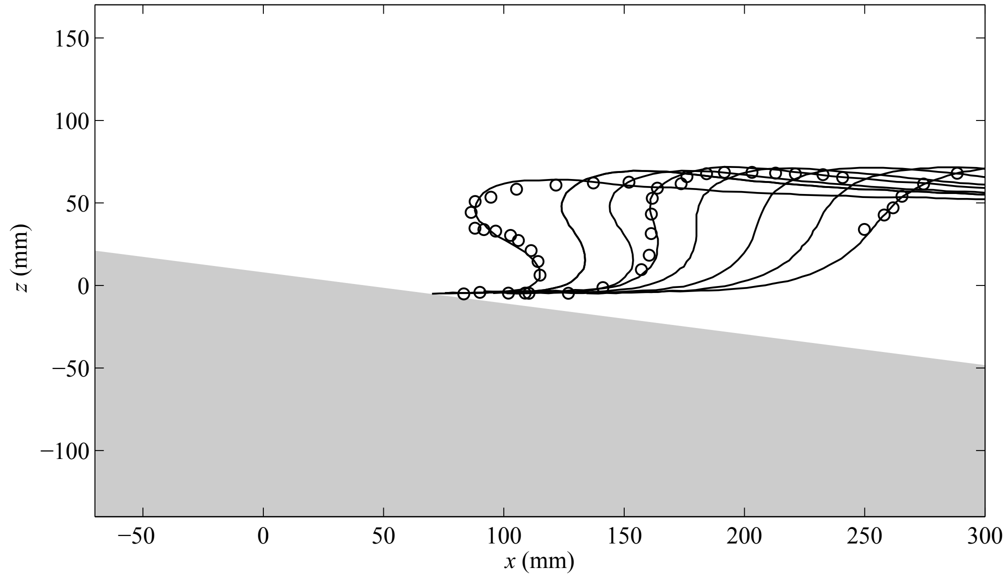

Figure 8: Comparison of numerical and experimental free surface profiles at different time instants. circles: experimental data; solid line: present numerical results

crest in the proximity of the interface. The wave height decreases as the wave approaches the shore after the breaking point. This implies that the overturned wave crest falls over the free surface in order to balance the change in the local momentum during the wave breaking process. Moreover, the numerical results agree well with the measured data for the changes in the wave profile and the horizontal velocity.

4.1.4 Solitary wave interaction with a slender circular cylinder

In order to validate the numerical model performance for simulating the solitary breaking wave interaction with a slender circular cylinder, the numerical results are compared with the experimental data. Figs. 9 and 10 show the numerical and laboratory wave profiles at $t\sqrt{g/d_0}$=31.70 and 32.18 and the corresponding normalized horizontal component of velocity profiles at x=0.32m, 0.36m and 0.41m, respectively. A rise in the water level along the upstream surface of the cylinder is observed as the wave interacts with the cylinder as shown in Fig. 10 (b). As mentioned in Section 4.1.3, the computed horizontal velocity profiles close to the seabed is strongly influenced by the boundary layer effect.

Fig. 11 shows the simulated horizontal and vertical components of velocity variation under the solitary wave during the initial interaction with the cylinder. The horizontal velocity profiles at different locations for $t\sqrt{g/d_0}$=31.70 and 32.18 show an increasing trend from the sea bottom towards the free surface as seen in Fig. 11 (a). However, the vertical velocity profiles show an increasing trend to the free surface for $t\sqrt{g/d_0}$=31.70 at x=0.32m and 0.36m (Fig. 9 (c)) and for $t\sqrt{g/d_0}$=32.18 at x=0.32m (10 (c)) and a decreasing trend for $t\sqrt{g/d_0}$=31.70

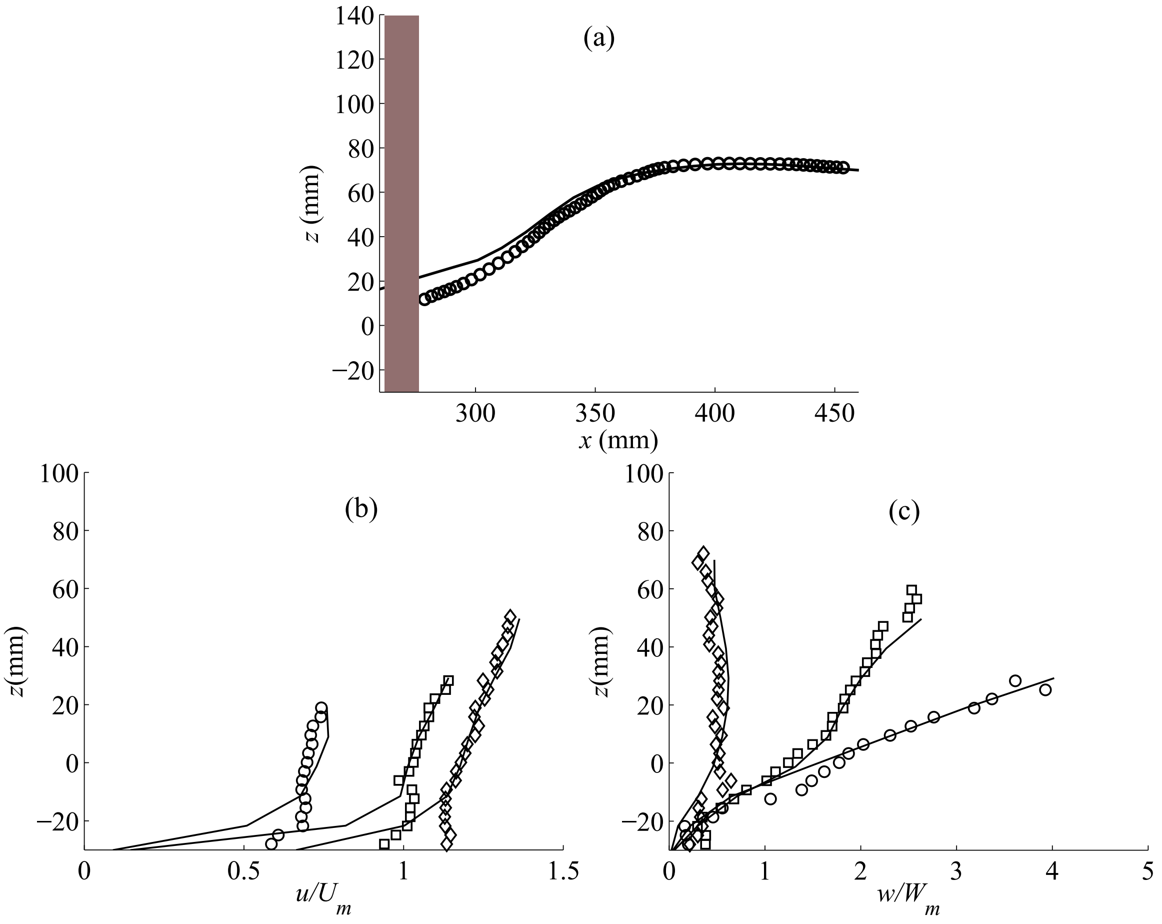

Figure 9: Comparison of numerical (solid lines) and experimental results for (a) wave surface elevation at $t\sqrt{g/d_0}$=31.70 (circles: experimental data), (b) horizontal velocity profiles and (c) vertical velocity profiles at x=0.32m (circles: experimental data), 0.36m (squares: experimental data) and 0.41m (diamonds: experimental data); U_m=605 mm/s and W_m=105 mm/s, W_m is the computed mean vertical velocity.

at x=0.41m (Fig. 9 (c)) and for $t\sqrt{g/d_0}$=32.18 at x=0.36m and 0.41m (Fig. 10 (c)). The vertical component of the velocity near the sea bottom is larger than close to the free surface as seen in Fig. 11 (b). The simulated wave surface profile and the horizontal and vertical velocities match well with the laboratory measurements. The simulated horizontal and vertical velocities (Fig. 11) exhibit a similar variability as that of laboratory experiments.

Fig. 12 shows the comparison of the computed breaking force by the present numerical model and the numerical model by Mo et al. (2013). Though the present results match overall well with the results from Mo et al. (2013), the details near the secondary peak after the maximum load are not well captured in the numerical simulation. The upper part of the total force variation obtained from the present study shows a sharp and narrow pattern with a small secondary hump. It should be noted that Mo et al. (2013) modelled only half of the computational domain along the x-direction based on the symmetric flow field assumption,

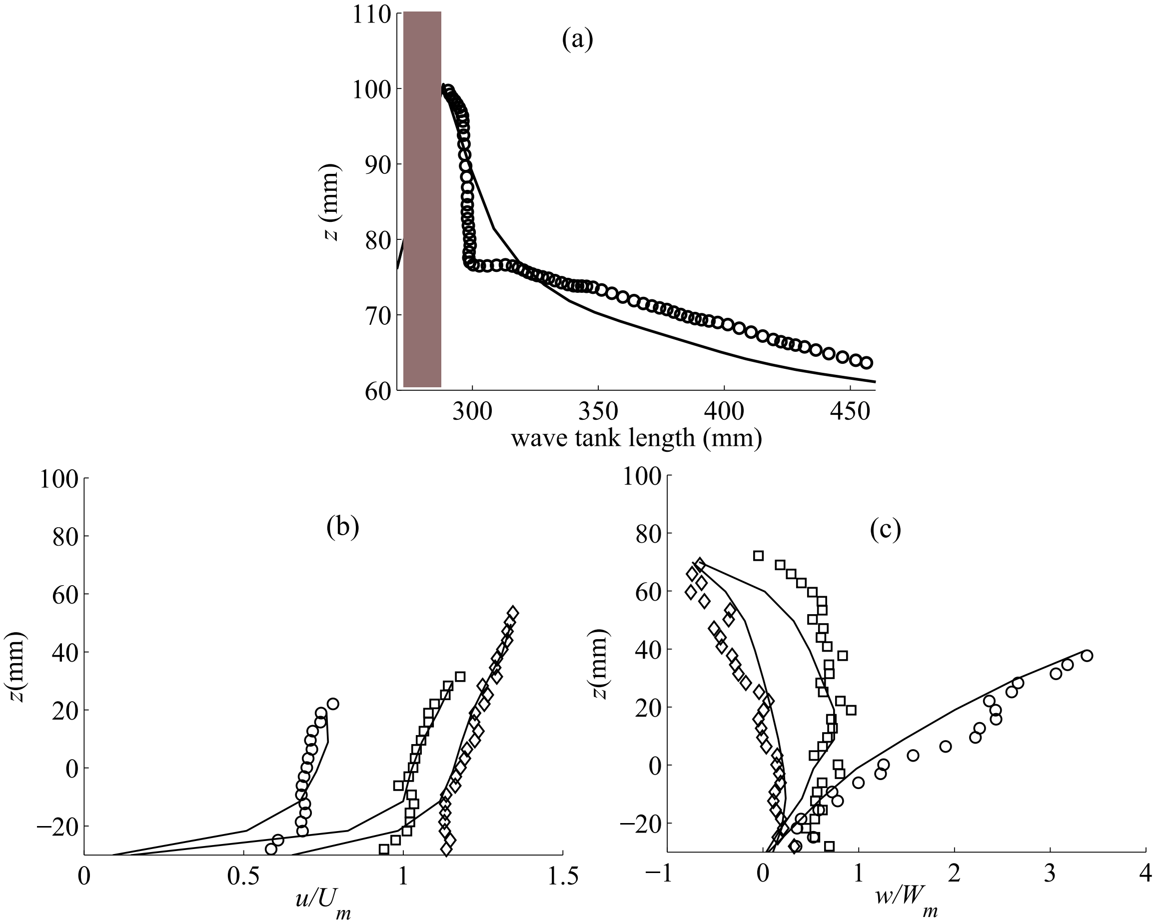

Figure 10: Comparison of numerical (solid lines) and experimental results for (a) wave surface elevation at $t\sqrt{g/d_0}$=32.18 (circles: experimental data), (b) horizontal velocity profiles and (c) vertical velocity profiles at x=0.32m (circles: experimental data), 0.36m (squares: experimental data) and 0.41m (diamonds: experimental data); U_m=644 mm/s and W_m=65 mm/s.

while the full computational domain is modelled in the present study. It seems likely that the flow features and the dynamic pressure gradient in the wake of the cylinder are not symmetric. Fig. 13 shows the velocity magnitude and the free surface changes of the wave interacting with the cylinder at different times. In the beginning, the water surface in front of the cylinder increases drastically (Fig. 13 (a)). The undisturbed upstream wave then separates into nearly two symmetric waves passing around the cylinder and the water level rises continuously until the flow around the cylinder is established (Fig. 13 (b)). As a result, the free surface deformation occurs along the surface of the cylinder and the water level decreases as the wave passes the cylinder. This is due to the reflection of the water column in front of the cylinder. Moreover, the water level rises with increase of the height of the water column that leads to the run-up effect (Fig. 13 (b)). This causes the early submergence of the cylinder and this in turn strongly influences the duration (t_d) of the impact and the maximum upstream pressure.

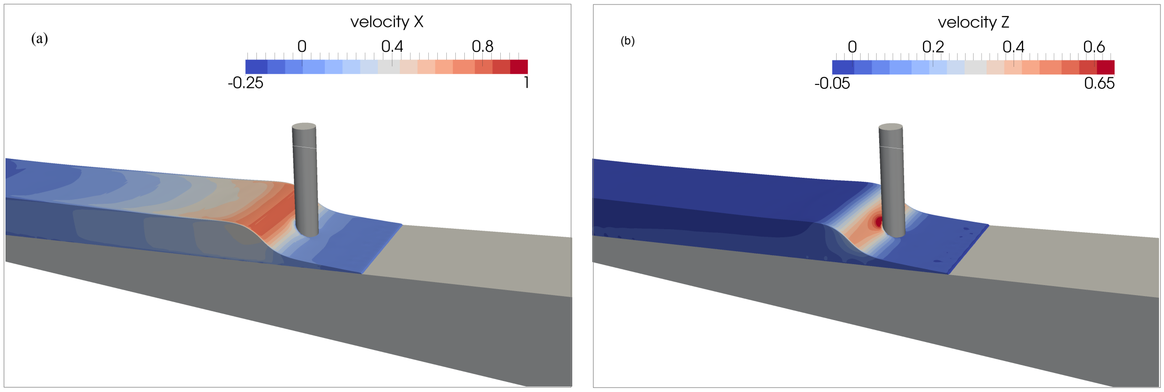

Figure 11: Simulated horizontal (V_x (m/s)) and vertical (V_z (m/s)) velocity variation at $t\sqrt{g/d_0}$=32.18 during the interaction.

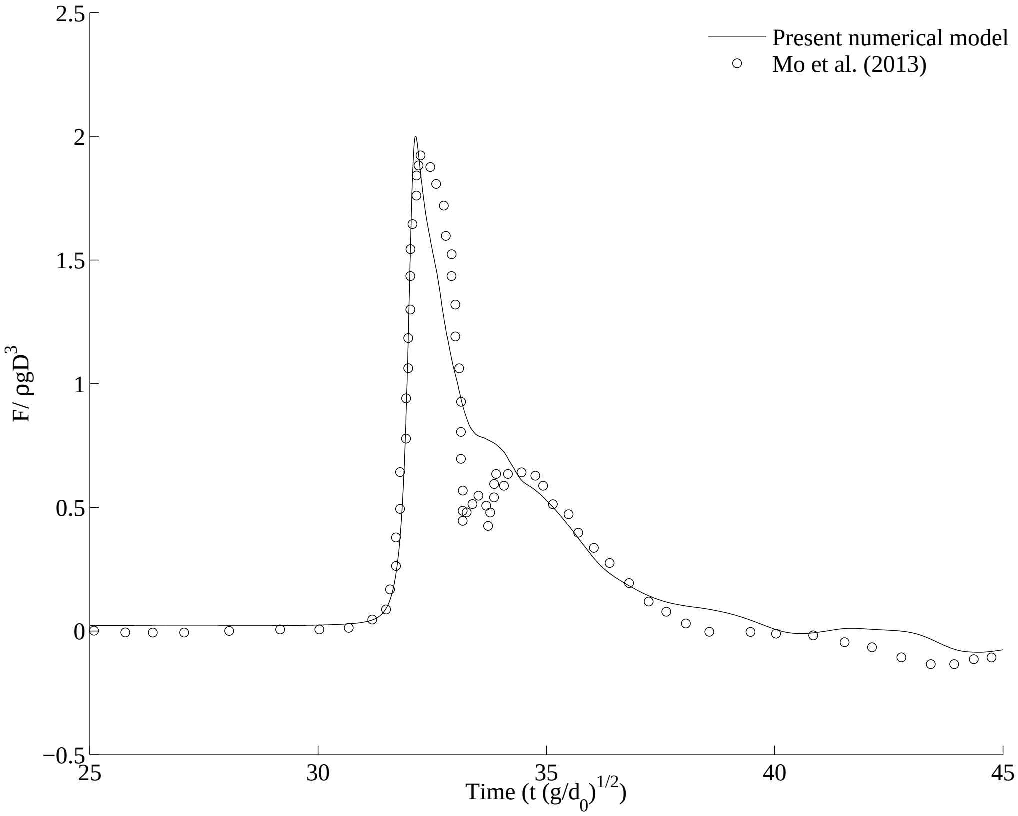

Figure 12: Comparison of present numerical and computational results by Mo et al. (2013) for total force on the cylinder

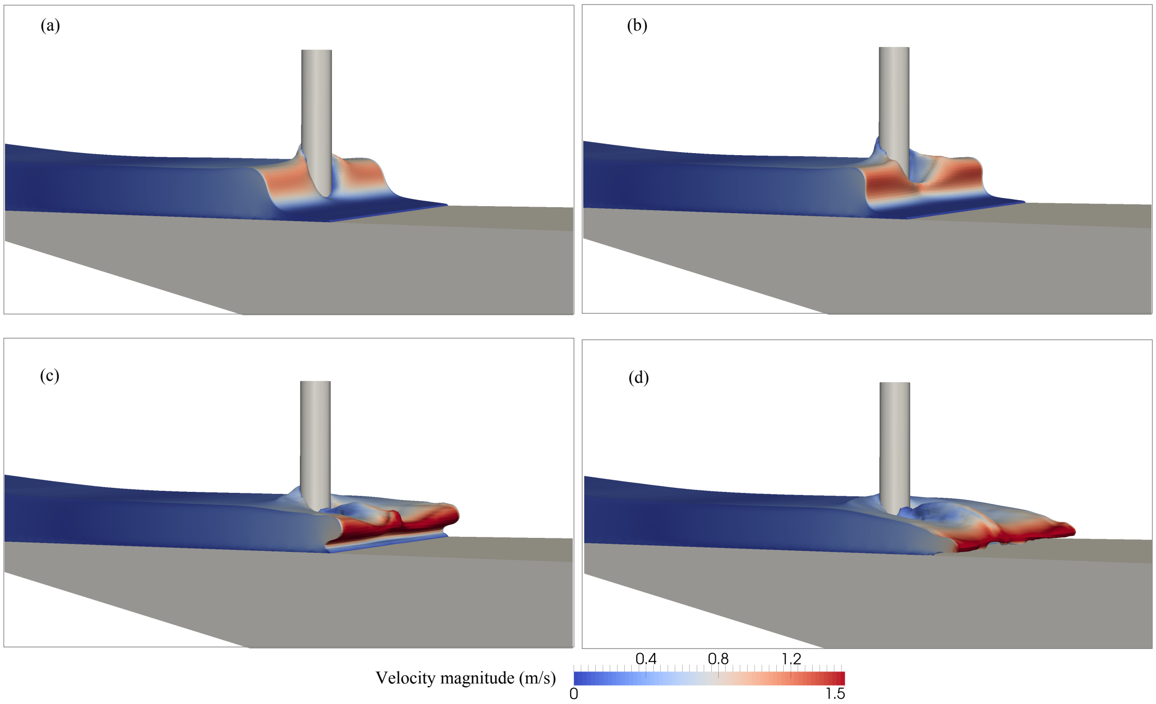

Figure 13: Simulated free surface changes with velocity magnitude variation for the benchmark case at t=7.50s (a), 7.55s (b), 7.65s (c) and 7.70s (d)

Further, the deformed free surface around the cylinder reconnects at the downstream side of the cylinder (Fig. 13 (c)). This evolves into a forward moving water jet behind the cylinder with high velocities near the free surface (Fig. 13 (d)).

4.1.5 Breaking wave force on a slender circular cylinder

The numerical model for simulating breaking wave forces is validated by comparing the experimentally measured breaking wave force on a vertical cylindrical pile by Chakrabarti et al. (1997). The authors investigated the wave loads from depth-limited breaking waves on a vertical single pile caisson. In the physical experiments, the cylinder has a uniform diameter D=0.046m up to 0.460m below the free surface and it is tapered over a distance of 0.08m to a uniform diameter D=0.052m. Whereas in the numerical simulation, a uniform diameter D=0.046m throughout its length is considered as the breaking wave force is strongly influenced by the free surface deformations around the cylinder. The computational set-up consists of a 4m long flat bed connected to a 1/50 slope followed by a 0.25m high flat bed as shown in Fig. 14. A cylinder with D=0.046m is placed at x=25.68m over a flat bed portion (Fig. 14). The size of the numerical wave tank is L_x=30m, L_y=0.30m, and L_z=1.80m and it is descretized into 13.80 million uniform cells with a grid size dx=0.01m. Fifth-order Stokes waves (Fenton, 1985) with H_0= 0.406m and T=3.0s are used in the numerical simulation. The water surface elevation is calculated at x=25.68m close to the cylinder (G1, Fig. 14).

Figs. 15 and 16 show the comparison of the computed and measured results for the water surface elevation (η) at x=25.68m (Fig. 14) and the breaking wave force (F), respectively. It appears that the computed η and F match well with the experimentally measured results

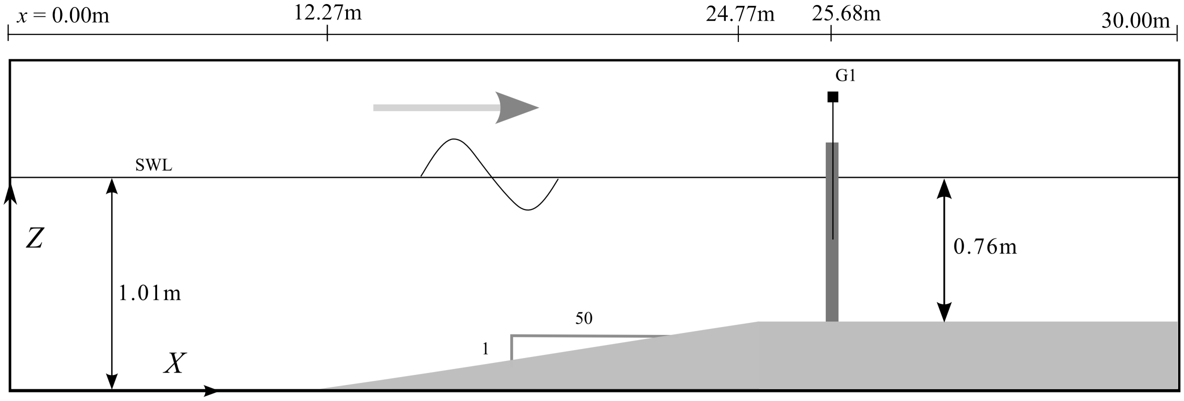

Figure 14: Numerical set-up.

by Chakrabarti et al. (1997). The breaking wave force on the cylinder is evaluated when the wave breaks at the cylinder. Though the computed wave crest is in good agreement with the experimental data, the wave trough is slightly over-predicted (Fig. 15). The development of the breaking wave force on a single pile caisson is well captured and the computed peak force distribution matches well with the measured one. However, the force emerged from the wave trough interaction with the cylinder is slightly under-predicted as seen in Fig. 16, but in general, the wave surface elevation (η) and the breaking wave force (F) are well represented in the numerical simulation.

4.2 Characteristics and geometric properties of solitary waves breaking over a sloping seabed

In this part the characteristics and geometric properties of solitary waves breaking over a slope are investigated for different H_0/d_0 (case B) with the 2D simulations. Fig. 17 (a) shows the relative breaker depth (d_b/d_0) versus the normalized wave heights (H_0/d_0) for different offshore wave heights (H_0) (since d_0 is fixed). It appears that d_b/d_0 increases with increasing H_0/d_0. As anticipated, waves with larger H_0/d_0 break earlier offshore at larger water depths as the shoaling rate increases with increasing wave heights. The range of d_b/d_0 for solitary waves in the present case is much lower than for periodic waves on slopes (Fig. 14 of Alagan Chella et al. (2015a)). Fig. 17 (b) and (c) show the breaker depth index (γ_b) and breaker height index (Ω_b) versus H_0/d_0 for different incident wave heights (H_0). It appears that γ_b and Ω_b decrease as H_0/d_0 increases. Waves with larger H_0/d_0 break seaward at larger water depths with relatively small increase in the incident wave height, corresponding to H_0/d_0=0.403, d_b/d_0=0.12 (Fig. 17 (a)), γ_b=3.63 (Fig. 17 (b)) and Ω_b=1.05 (Fig. 17 (c)). Waves with smaller H_0/d_0 shoal more over the slope and break farther shoreward at a smaller water depth with a relatively large change from the incident wave height, corresponding to H_0/d_0=0.257, d_b/d_0=0.051 (Fig. 17 (a)), γ_b=5.77 (Fig. 17 (b)) and Ω_b=1.136 (Fig. 17 (c)). In the present case, the range of γ_b is varied from 3.50 to 5.77, which are much larger than the typical values of periodic waves on slopes as presented in Fig. 16 of Alagan Chella et al. (2015a). This also suggests that in the case of solitary waves, the absence of the wave trough interaction with the slope cause the waves to propagate further up the slope, breaking at shallower water depths.

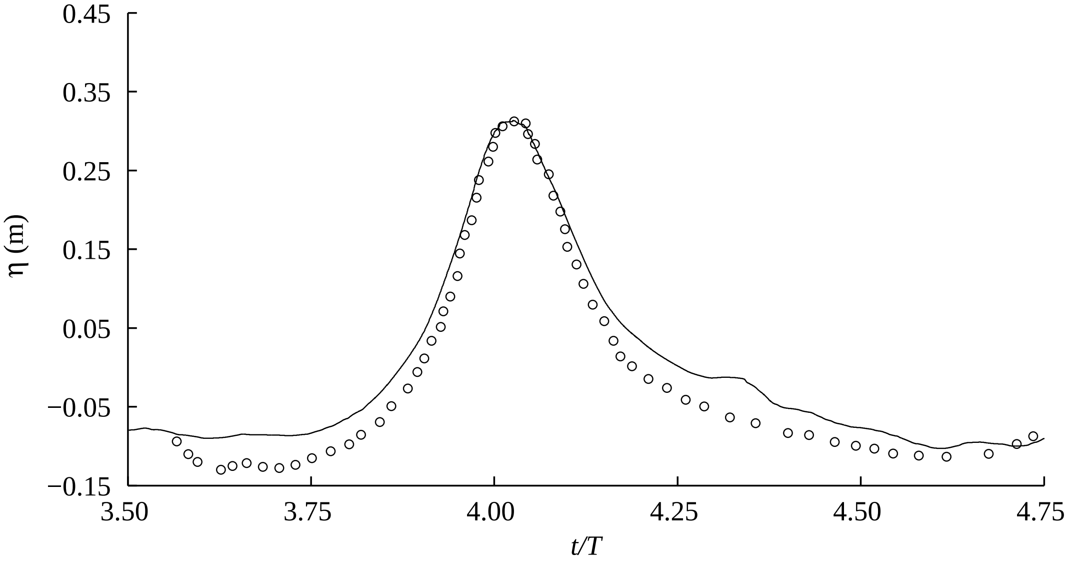

Figure 15: Comparison of present numerical and experimental results by Chakrabarti et al. (1997) for wave surface elevation close to the cylinder.

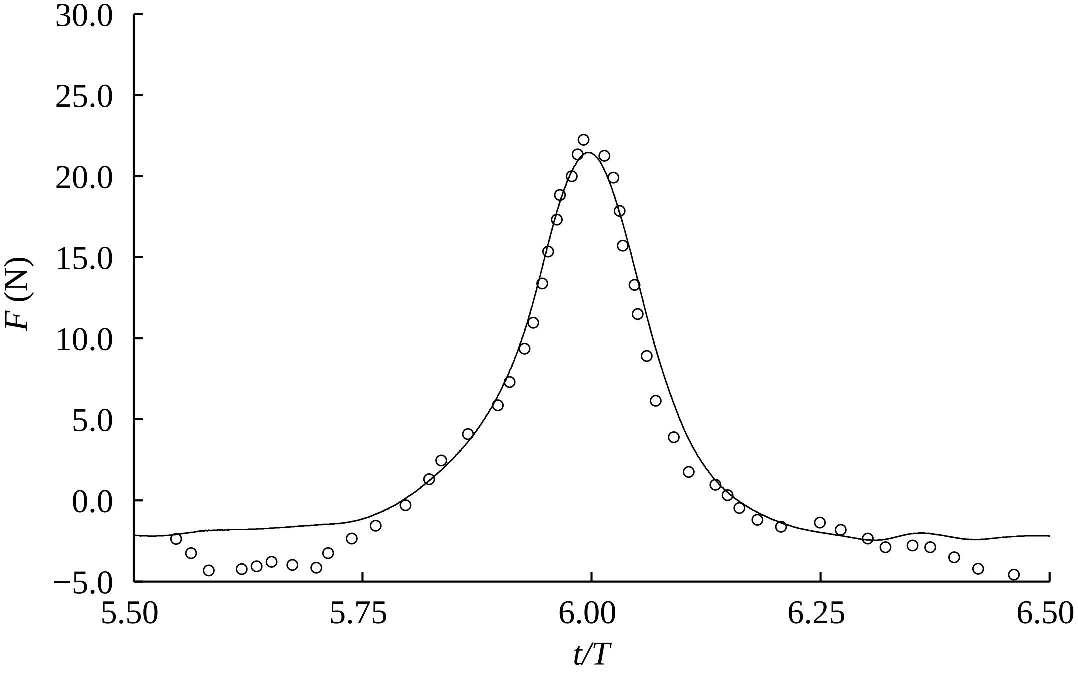

Figure 16: Comparison of present numerical and experimental results by Chakrabarti et al. (1997) for total force on the cylinder.

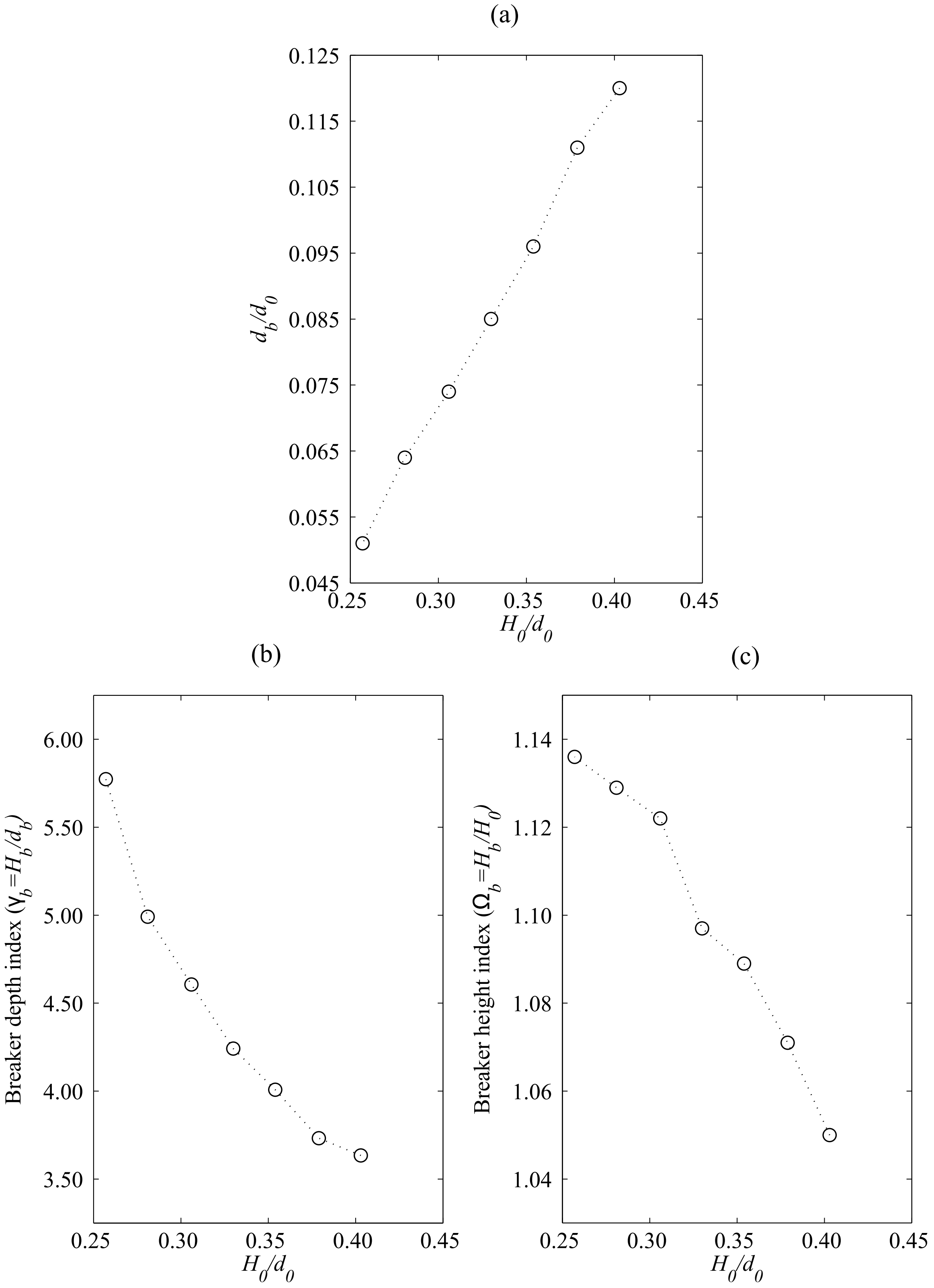

Figure 17: Computed (a) relative breaker depth (d_b/d_0), (b) breaker depth index (γ_b), and (c) breaker depth index (Ω_b) versus normalized wave height (H_0/d_0)

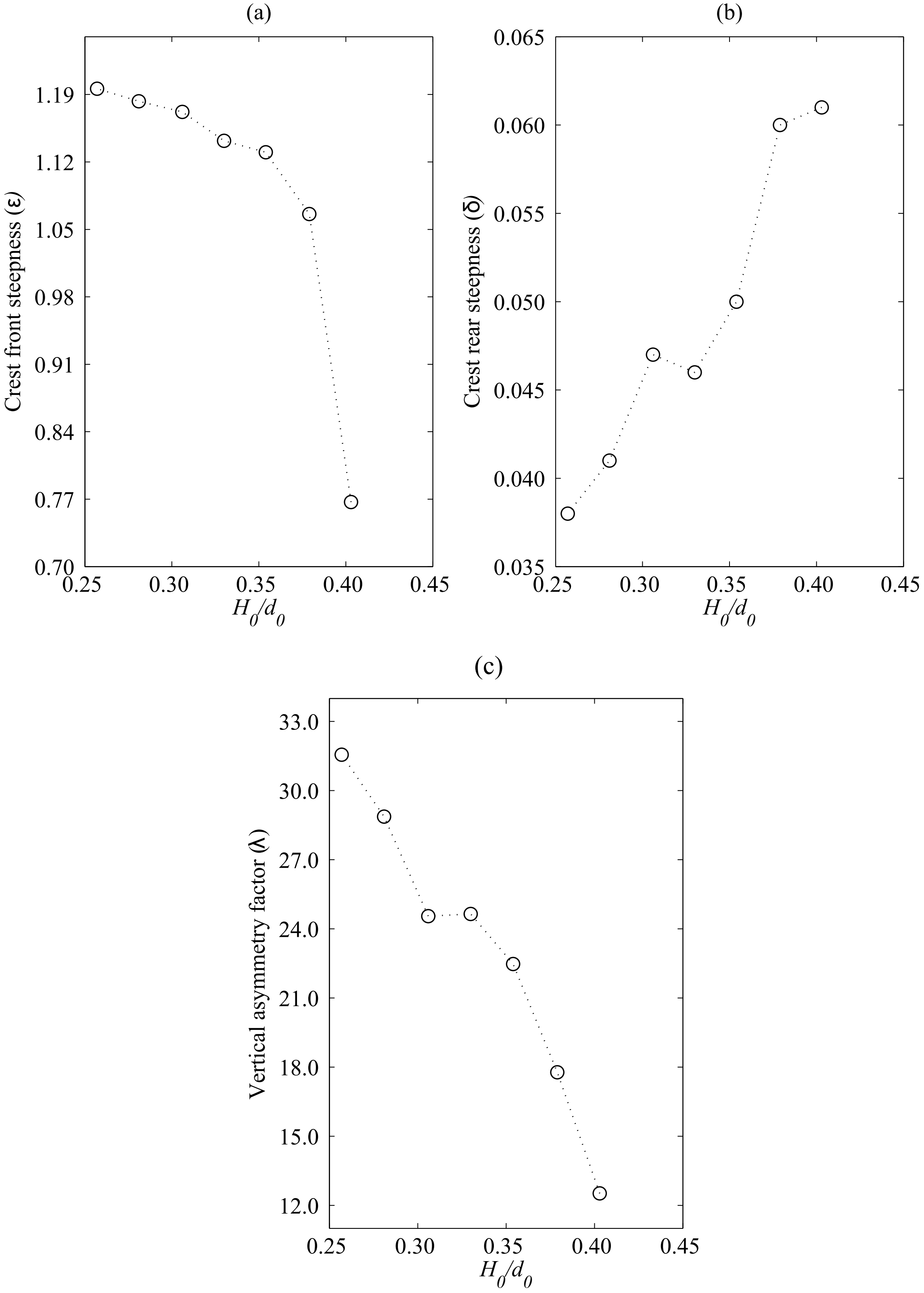

Figure 18: Computed (a) crest front steepness (ε), (b) crest rear steepness (δ) and (c) vertical asymmetry factor (λ) versus normalized wave height (H_0/d_0)

The geometric properties at breaking are calculated based on the wave crest front steepness (ε), the wave crest rear steepness (δ) and the vertical asymmetry factor (λ) proposed by Kjeldsen and Myrhaug (1978) as defined in Fig. 2. Moreover, the relationship between the wave characteristics and the geometric properties as well as the breaking force characteristics are discussed in Section 4.3.2. Fig. 18 shows ε, δ and λ versus the normalized wave height (H_0/d_0) for different offshore wave heights (H_0) (since d_0 is fixed). It appears that ε (Fig. 18 (a)) and λ (Fig. 18 (c)) decrease and δ (Fig. 18 (b)) increases as H_0/d_0 increases. Waves with larger H_0/d_0 do not undergo much deformation when compared to waves with smaller H_0/d_0. As seen from Fig. 18 (c), waves with smaller H_0/d_0 approaching the breaking point experience more deformation as smaller waves propagate longer over the slope than waves with larger H_0/d_0. This is consistent with the findings of Grilli et al. (1997) who investigated the characteristics of solitary waves over slopes. The front face of the wave steepens and the rear face of the wave becomes milder as the incident wave height increases, corresponding to H_0/d_0=0.257, ε=1.20 (Fig. 18 (a)), δ=0.038 (Fig. 18 (b)) and λ=31.56 (Fig. 18 (c)). The range of λ from 12.0 to 31.56 is larger than that of periodic waves in shallow water as shown in Fig. 24 of Alagan Chella et al. (2015a).

4.3 Breaking solitary wave forces on a vertically mounted slender circular cylinder

4.3.1 Breaking solitary wave force variation for different cylinder positions

In this part the effect of the relative distance between the cylinder and the breaking point on the breaking wave forces is examined for different cylinder positions. The cylinder is placed at different locations based on the normalized relative cylinder distance $L_c = H_b x_c / d_b D$, where x_c is the distance between the cylinder and the breaking point. The normalized relative cylinder distance (L_c) describes the relationship between the breaker depth index ($\gamma_b = H_b/d_b$), the diameter (D) and the distance between the breaking point and the cylinder (x_c). A total of 9 simulations are carried out for the L_c values listed in Table 1 (case A). Fig. 19 depicts the velocity variation and the free surface changes at the selected positions of the cylinder during the breaking process. For a given wave, the variation of the maximum force for non-breaking, breaking and post-breaking waves is evaluated by placing the cylinder at different normalized relative distances corresponding to L_c=0.0 (at breaking, Fig. 19 (f)), L_c=4.24, 8.48, 12.72, 16.96 and 21.20 (before breaking, Figs. 19 (a) to (e)) and L_c=-4.24, -8.48 and -12.72 (after breaking, Figs. 19 (g) to (i)) as listed in Table 1.

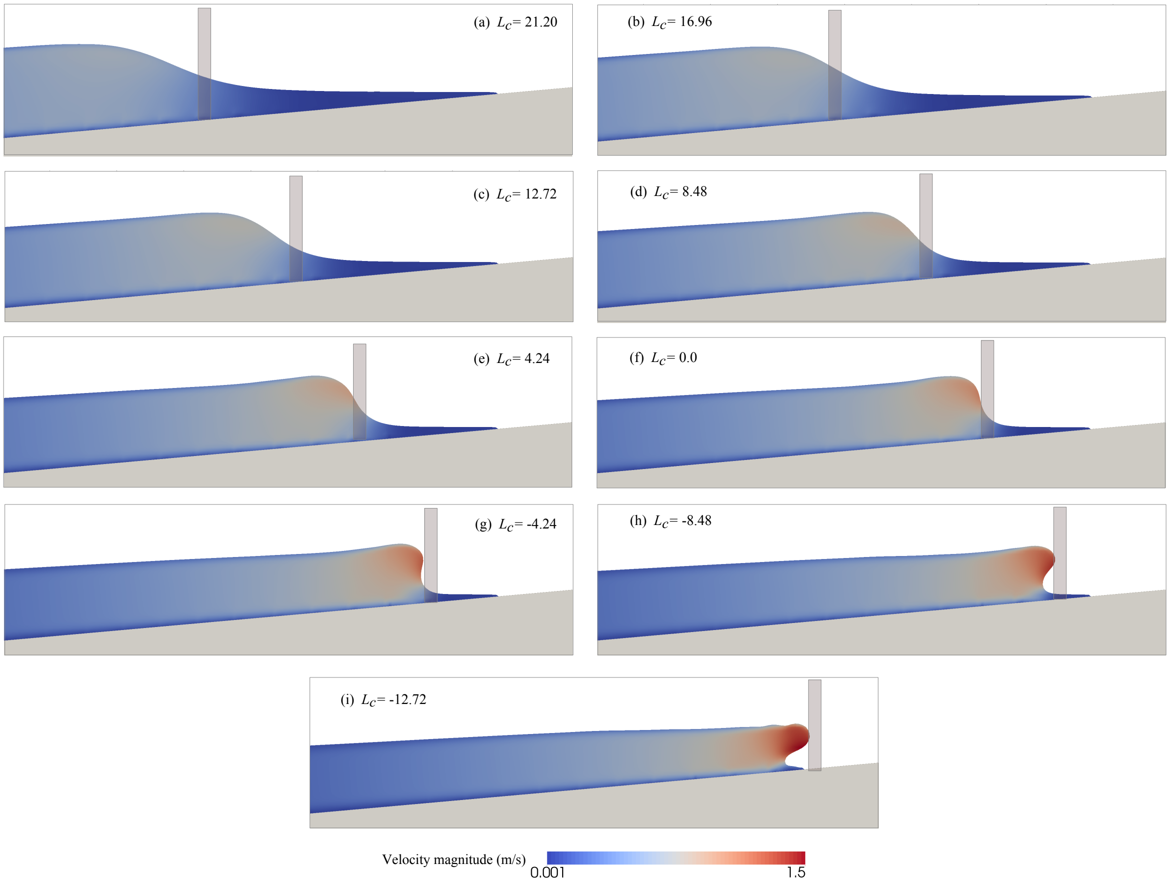

Figure 19: Simulated free surface profiles with velocity magnitude (m/s) variation at t=5.38s (a), 5.51s (b), 5.57s (c), 5.67s (d), 5.74s (e), 5.80s (f), 5.87s (g), 5.94s (h), and 6.00s (i) and the corresponding cylinder positions, see case A in Table 1.

Figs. 20 and 21 show the normalized wave force ($F_{norm} = F/\rho g D^3$) versus time for different normalized relative distances (L_c) before and after the breaking point. The maximum normalized force occurs when the cylinder is placed just before the breaking point at L_c=4.24 (Fig. 19 (e) and Fig. 20 (e)), which is larger than the wave force experienced by the cylinder when it is placed at the breaking point (L_c=0.0) (Fig. 19 (f) and Fig. 21 (a)). It appears that the wave with the inclined wave front is less steep leading to a larger submergence of the cylinder, causing a larger force than the force caused by a steeper wave with a smaller submergence of the cylinder. Table 2 presents the computed peak force (F_{peak}), impact duration (t_d), and rise time (t_r) for different normalized relative distances (L_c). It appears that the impact duration (t_d) and rise time (t_r) increase as L_c increases (from L_c=21.20 (before breaking) to L_c=-12.72 (after breaking)). The corresponding cylinder locations are presented in Fig. 19. The impact duration (t_d) and rise time (t_r) are 0.259s and 0.059s, respectively, for L_c=4.24, and 0.184s and 0.056s, respectively, for L_c=0.00. Although the impact duration (t_d) is larger for L_c=4.24 (Fig. 20 (e)) than for L_c=0.0 (Fig. 21 (a)), the rise time (t_r) is almost the same for both cases. The main differences between the case with L_c=0.0 (Fig.

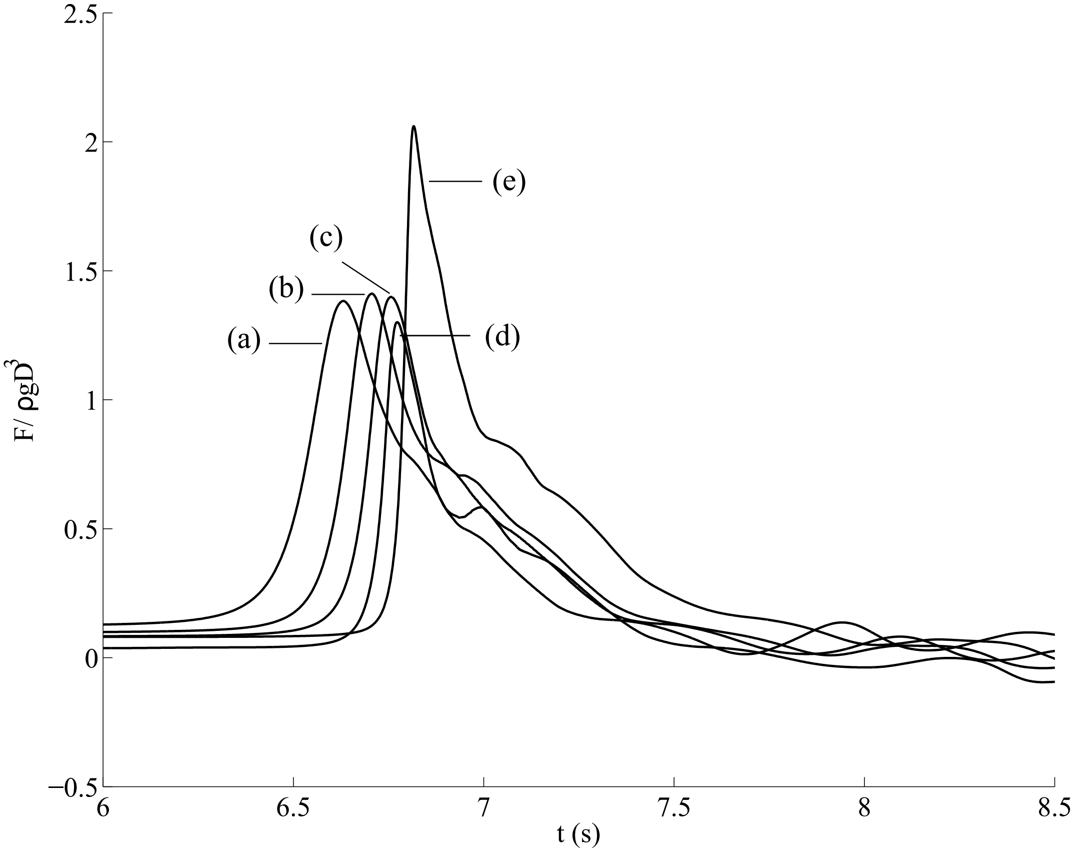

Figure 20: Computed normalized force ($F_{norm} = F/\rho g D^3$) versus time for different normalized relative distances $L_c = (H_b x_c/d_b D)$ (before breaking): (a) 21.20, (b) 16.96, (c) 12.72, (d) 8.48 and (e) 4.24

19 (f)) and L_c=4.24 (Fig. 19 (e)) are the local steepness of the wave front, larger impact duration (t_d), and the submergence of the cylinder during the impact. Therefore, a certain combination of the cylinder submergence and the deformed wave shape causes the maximum horizontal force. It is also found that the wave height at which the maximum horizontal force occurs is almost the same as that of the wave height at the breaking point. This also implies that the relative distance between the cylinder and the breaking point plays a crucial role in obtaining the maximum force.

Simulation cases	Normalized wave height, H_0/d_0	Normalized relative distance, $L_c = (H_b x_c/d_b D)$	Peak force, F_{peak} (N)	Impact duration, t_d (s)	Impact rise time, t_r (s)
1		-12.72	3.56	0.068	0.021

0.33

2		-8.48	3.68	0.081	0.021
3		-4.24	2.67	0.107	0.023
4		0.00	3.36	0.184	0.056
5		4.24	4.35	0.259	0.058
6		8.48	2.85	0.320	0.099
7		12.72	2.95	0.428	0.142
8		16.96	2.98	0.464	0.175
9		21.20	2.92	0.63	0.214

Table 2: Computed force peak (F_{peak}), Impact duration (t_d), and Impact rise time (t_r) for different normalized distances (L_c).

The steepness of the wave front and the crest particle velocity increases as the wave propagates over the slope. Thus, a portion of wave crest propagates faster than the rest of the wave with an ejected forward water jet as presented in Fig. 19 (h) and (i). Therefore, the overturned wave crest impinges onto the surface of the cylinder causing a very short duration impact, corresponding to Fig. 21 (c) and (d) and Fig. 19 (h) and (i). It is noticed that the development of the overturned wave crest after breaking is associated with a smoothly ejected water jet (Fig. 19 (h) and (i)) and the velocity distribution under the wave crest is almost constant. The impact duration (t_d) and rise time (t_r) are 0.081s and 0.021s, respectively, for L_c=-8.48, and 0.068s and 0.021s , respectively, for L_c=-12.72. The peak force (F_{peak}) and impact rise time (t_r) are almost the same for both cases; however, the impact duration (t_d) is larger for L_c=-8.48.

When the wave breaks just before the cylinder, the maximum force on the cylinder computed at L_c=-4.24 (Figs. 19 (g) and 21 (b)) is smaller than the non-breaking wave force. This may be due to the interaction of an overturned wave crest including an air pocket evolved during the breaking process with the cylinder as shown in Fig. 19 (g). In the case of L_c=-8.48 (Fig. 19 (h)) and L_c=-12.72 (Fig. 19 (i)), the wave breaks far before the cylinder and it experiences the maximum force from the impingement of the wave crest with the ejected water jet on the cylinder. Therefore, the total forces acting on the cylinder at L_c=-8.48 (Fig. 21 (c)) and -12.72 (Fig. 21 (d)) are larger than for the non-breaking wave forces for L_c=0.0, (Fig. 19 (f)), L_c=4.24 (Fig. 19 (e)).
As can be seen from Fig. 19, the slope of the wave front increases as L_c increases. During the wave impact, the rise time (t_r) mainly depends on the local slope of the wave front (Sawaragi and Nochino, 1984). The computed results indicate that t_r decreases as the front shape of the wave becomes steeper. Moreover, the present numerical results confirm the experimentally measured characteristics reported by Sawaragi and Nochino (1984) who investigated wave impact forces on a vertical slender cylinder experimentally. Finally, Fig. 22 presents the normalized maximum force ($F_{maxn} = F_{max}/\rho g D^3$) versus L_c for different cylinder positions, i.e. showing the peak values of the curves shown in Figs. 20 and 21 versus L_c. The corresponding peak forces (F_{peak}) for each L_c case are listed in Table 2. The results demonstrate that L_c plays an important role in determining the maximum force. This is also consistent with the experimental observations by Wienke et al. (2000) and Irschik et al. (2002) who investigated the breaking wave forces on a slender cylinder.

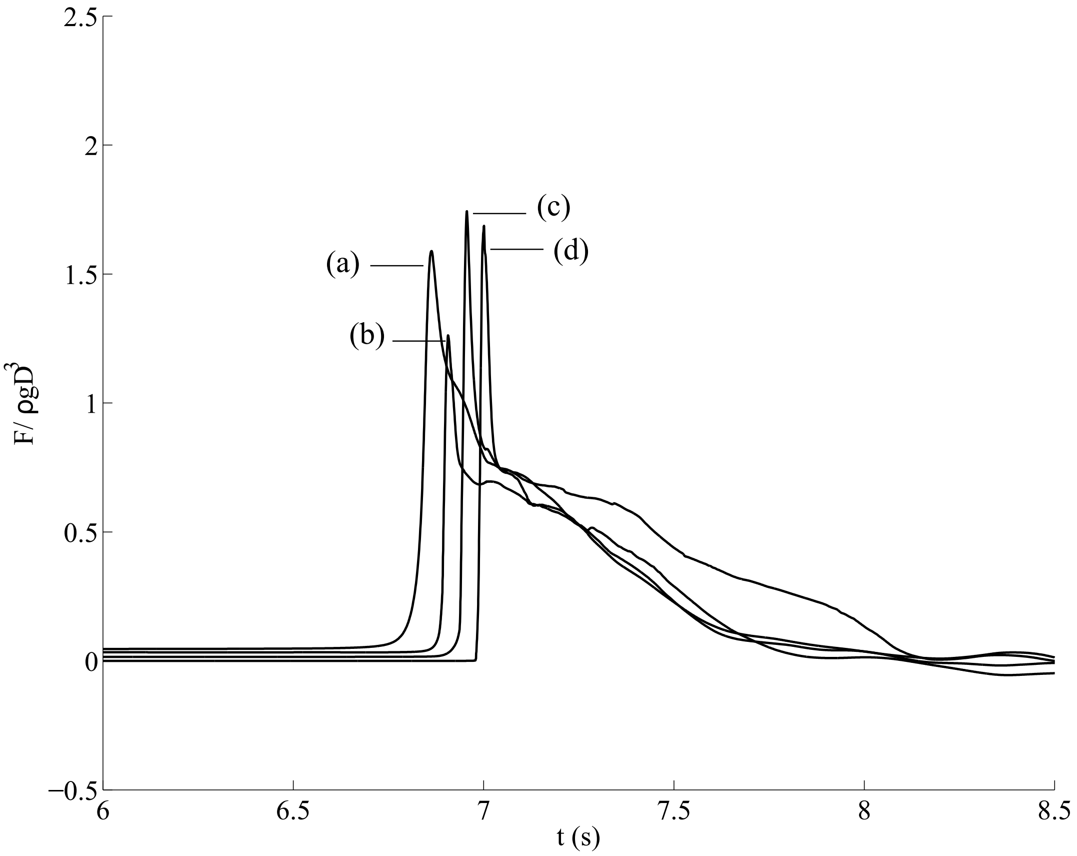

Figure 21: Computed normalized force ($F_{norm} = F/\rho g D^3$) versus time for different normalized relative distances $L_c = (H_b x_c/d_b D)$ (after breaking): (a) 0.0, (b) -4.24, (c) -8.48, and (d) -12.72.

4.3.2 Breaking solitary wave force variation for different incident waves

Further, a total of seven simulations are carried out to study the characteristics of breaking wave forces for different incident waves as seen in Table 1 (case B). The cylinder is placed based on the normalized relative distance $L_c = H_b x_c/d_b D$=4.24 corresponding to the maximum total force for each case. The breaking locations obtained from the 2D simulations are used to determine the appropriate relative cylinder position. Fig. 23 shows the normalized wave force (F_{norm}) versus time for different normalized incident wave heights (H_0/d_0). As expected, the results show that F_{norm} increases as H_0/d_0 increases for larger incident waves. Table 3 presents the computed peak force (F_{peak}), impact duration (t_d), rise time (t_r), and force impulse (I_{td}, Fig. 1) over the impact duration for different normalized incident wave heights (H_0/d_0). It appears that t_d, t_r, and I_{td} decrease and F_{peak} increases as H_0/d_0 increases. It is noticed that the area under the primary peak of the normalized total force curve becomes larger and the shape of the primary peak becomes narrower as H_0/d_0 increases.

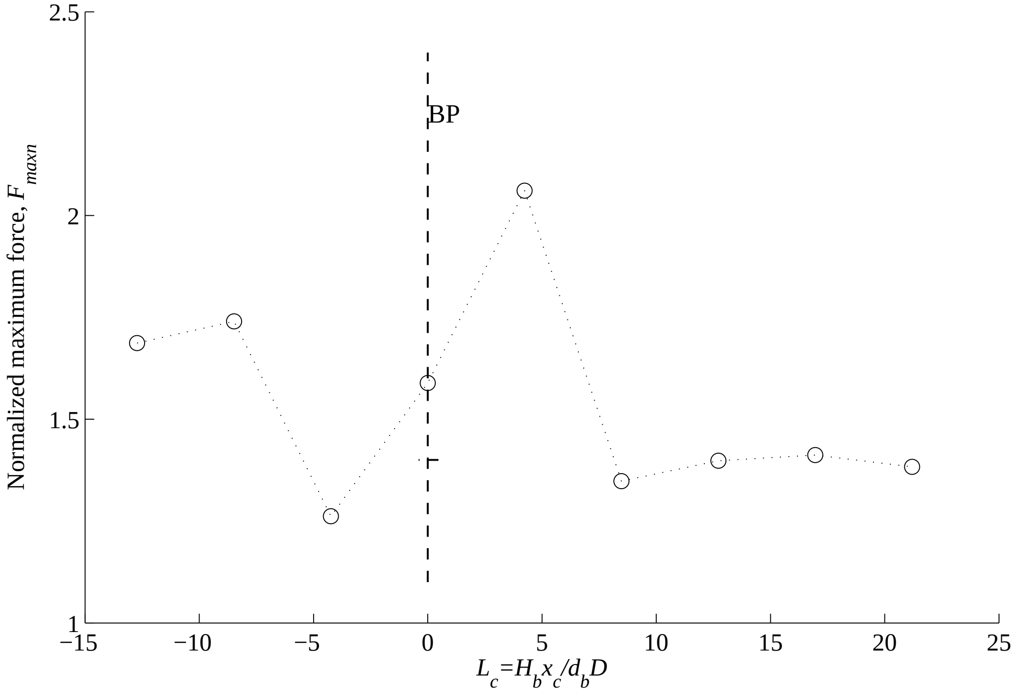

Figure 22: Computed normalized maximum force ($F_{maxn} = F_{max}/\rho g D^3$) as a function of $L_c = H_b x_c/d_b D$, BP is the breaking point.

Simulation cases	Normalized wave height, H_0/d_0	Normalized relative distance, $L_c = (H_b x_c/d_b D)$	Peak force, F_{peak} (N)	Impact duration, t_d (s)	Impact rise time, t_r (s)	Force impulse, I_{td} (Ns)
1	0.257	4.24	3.14	0.440	0.095	0.690
2	0.281		3.82	0.352	0.062	0.692
3	0.305		4.31	0.328	0.062	0.697
4	0.33		4.36	0.300	0.060	0.690
5	0.354		4.53	0.255	0.059	0.544
6	0.378		5.12	0.240	0.052	0.620
7	0.403		5.25	0.118	0.042	0.442

Table 3: Computed force peak (F_{peak}), Impact duration (t_d), Impact rise time (t_r), and force impulse (I_{td}) for different normalized wave heights (H_0/d_0).

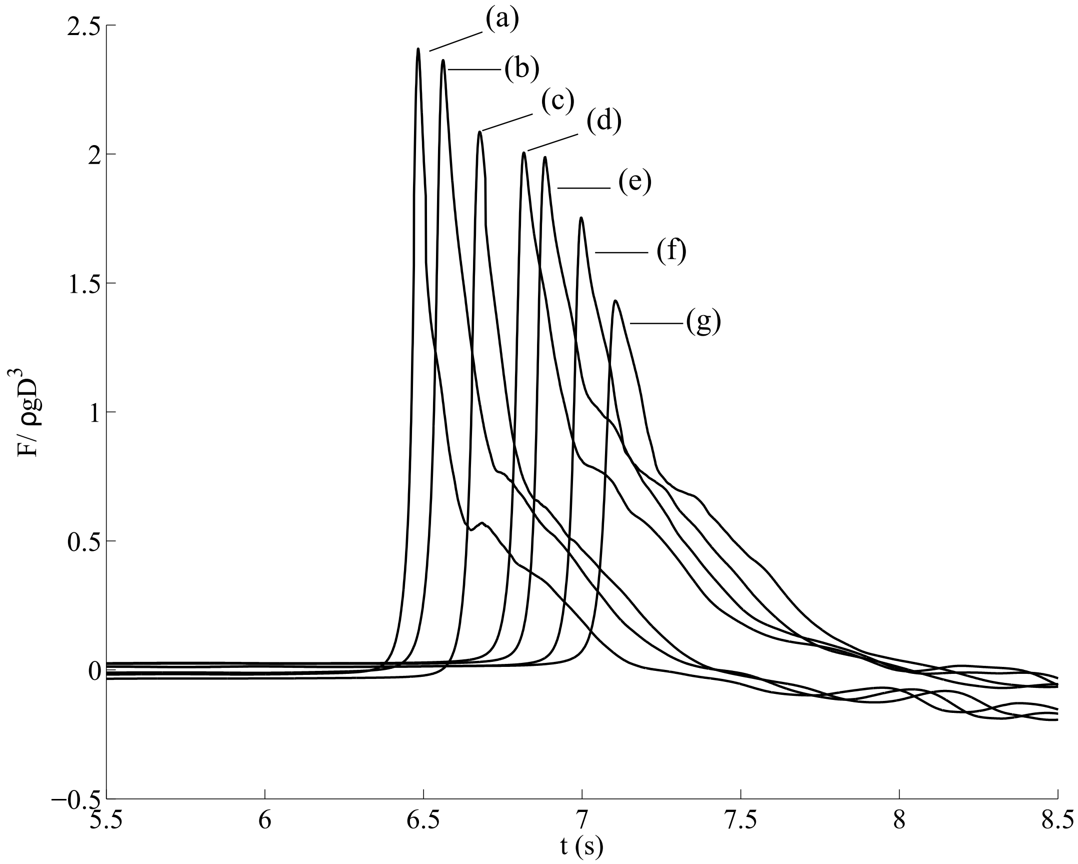

Figure 23: Computed normalized total force (F_{norm}) versus time for different H_0/d_0: (a) 0.403, (b) 0.378 (c) 0.354 (d) 0.330, (e) 0.305, (f) 0.281 and (g) 0.257

On the one hand, the cylinder experiences a larger peak force (F_{peak}) of a shorter rise time (t_r) with a lower force impulse (I_{td}) from a larger incident wave, corresponding to H_0/d_0=0.403, F_{peak}=5.25N, t_r=0.042s, and I_{td}=0.442 Ns in Table 3. Further, the crest front steepness (ε) and the vertical asymmetry factor (λ) become lower, implying that the wave front does not deform much during the shoaling, corresponding to H_0/d_0=0.403, ε=0.76 (Fig. 18 (a)), λ=12.0 (Fig. 18 (c)), Ω_b=1.048 (Fig. 17 (c)). On the other hand, for smaller incident waves, F_{peak} decreases and t_r and I_{td} increase, corresponding to H_0/d_0=0.257, F_{peak}=3.14N, t_r=0.085s, and I_{td}=0.69 Ns in Table 3. Then, ε=1.20 (Fig. 18 (a)) and λ=31.56 (Fig. 18 (c)) increase as H_0/d_0 decreases. This also suggest that the forces due to smaller incident waves rise slowly for longer duration with larger force impulses. As reported by Hattori et al. (1994) who studied breaking wave impact pressure on a vertical wall experimentally, the force impulse increases as the rise time (t_r) increases. The authors also pointed out that a larger load on a vertical wall is always associated with a lower peak force and a larger force impulse. Overall, the computed variations of F_{peak} versus t_r and F_{peak} versus I_{td} are quite consistent with the previous studies on vertical walls (Hattori et al., 1994; Kortenhaus et al., 1999; Cuomo et al., 2010, 2011)

Though a larger incident wave does not undergo more deformation during the shoaling, i.e. the wave front is not steeper than for a smaller incident wave at breaking, the impact rise time (t_r) is smaller with the lower force impulse (I_{td}). However, the slope of the wave front always determines the rise time (Sawaragi and Nochino, 1984). The computed geometric properties indicate that larger incident waves have sharper rear parts, whereas smaller incident waves have smoother rear parts. It is therefore likely that the large crest particle velocity changes occur rapidly when a larger incident wave interacts with the cylinder, causing a sudden rise of the impact force, i.e. lower impact rise time (t_r).

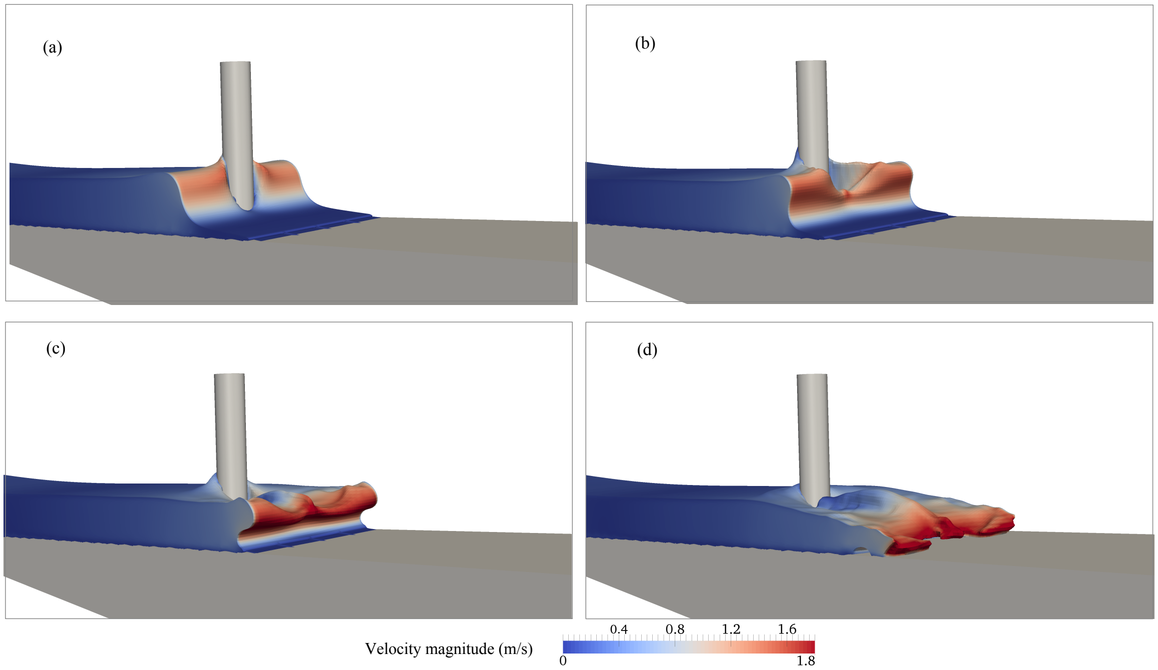

Figure 24: Simulated free surface changes with velocity magnitude (m/s) variation during the interaction of the larger solitary wave (H_0/d_0=0.403) with the cylinder at t=6.37s (a), 6.56s (b), 6.75s (c) and 6.94s (d)

Fig. 24 shows the velocity magnitude and free surface variation at different stages for the interaction of the largest solitary wave (H_0/d_0=0.403, Fig. 23 (a)) with the cylinder. The free surface deformation around the cylinder becomes wider and larger for larger solitary waves (Fig. 24 (a) and (b)) when compared to the interaction with relative smaller solitary waves (Fig. 13 (a) and (b)). This creates a larger pressure gradient downstream and the run-up upstream (Fig. 24 (a) and (b)). In addition to that, the high crest velocity can cause the wave to pass the cylinder more quickly with a large pressure gradient resulting in a larger impact force. The size of the downstream water jet formed during the reconnection of the free surface behind the cylinder (Fig. 24 (c) and (d)) grows larger and wider as H_0/d_0 increases. This also implies that the free surface deformation in the vicinity of the cylinder increases as the incident wave height increases.

Fig. 25 shows the average slamming coefficient ($\overline{C_s}$) as defined in Eq. 7 versus the normalized wave height (H_0/d_0) for different offshore wave heights (H_0) (since d_0 is fixed). The variation of $\overline{C_s}$ shows a decreasing trend as H_0/d_0 increases which is opposite to the variation of F_{norm} versus H_0/d_0 (see Fig. 23) and similar to the variation of I_{td} and t_r versus H_0/d_0 (Table 3). Waves with larger H_0/d_0 break farther offshore at shallower water depths with small changes in the wave crest, corresponding to H_0/d_0=0.403, d_b/d_0=0.12 (Fig. 17 (a)), γ_b=3.63 (Fig. 17 (b)) and Ω_b=1.05 (Fig. 17 (c)). Therefore, the cylinder exposed to smaller incident waves experiences larger force impulse and larger force from the deformed wave above the still water level, corresponding to H_0/d_0=0.257, γ_b=5.77 (Fig. 17 (b)), ε=1.196 (Fig. 18 (a)), λ=31.56 (Fig. 18 (c)), and I_{td}=0.690Ns (Table 3). On the other hand, $\overline{C_s}$, I_{td}, and t_r decrease and F_{peak} increases as H_0/d_0 increases. In addition to that the submerged projected area (Eq. 7) of the cylinder and the crest velocity increase with the increase of H_0. An implication of this is the possibility that the force contribution from the wave above the still water level to the total force increases as the incident wave becomes smaller. Consequently, the average slamming coefficient ($\overline{C_s}$) decreases as H_0 increases. The present results suggest that $\overline{C_s}$ and I_{td} represent an important part of the force contribution from the wave above the still water level to the total force.

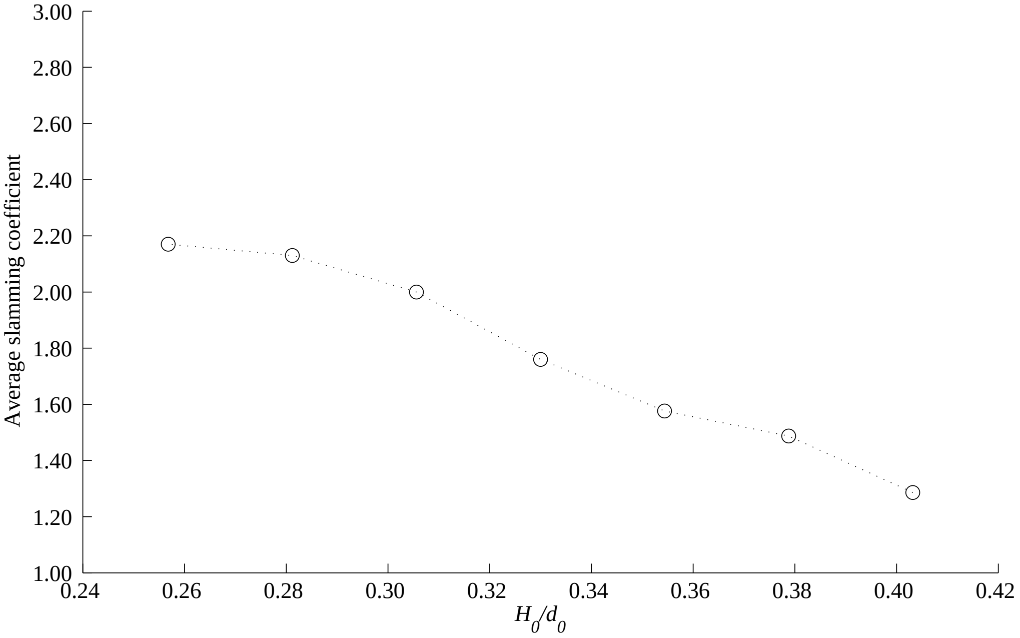

Figure 25: Computed average slamming coefficients ($\overline{C_s}$) versus normalized wave height (H_0/d_0)

5 Conclusions

Numerical simulations have been carried out with the CFD model, REEF3D to study breaking solitary waves and the associated wave impact forces on a slender cylinder over a sloping seabed. The performance of the numerical model is evaluated against the experimental data for the wave generation, wave surface elevation, free surface profile, horizontal and vertical velocity profiles reported by Mo et al. (2013) and breaking wave forces reported by Chakrabarti et al. (1997).

The main purpose of the present study is to investigate the characteristics and geometric properties of breaking solitary waves and their relationship with the breaking wave forces on a cylinder over a sloping seabed. Further, the study investigates the significance of the relative distance between the breaking point and the cylinder on the breaking wave forces on the cylinder. The breaking wave force characteristics such as the peak impact force, the impact duration and rise time, the average slamming coefficient, and the force impulse are also examined to understand the underlying physical processes. However, to the authors′ knowledge no data to compare this second part with are available in the open literature, but the results suggest that the numerical model can represent important flow features related to breaking solitary waves and the interaction with a vertical cylinder. The main results are:

- The breaker depth index and the breaker height index for solitary waves on slopes have a similar trend as breaking periodic waves on slopes. However, the breaker depth index for solitary waves is much larger than typical values for periodic waves. This suggests that for a given slope, a solitary wave propagates further up on the slope and breaks in a shallower water depth than periodic waves.

- Solitary waves with smaller incident wave heights deform more during the shoaling and break at shallower water depth with larger breaker height due to the longer interaction time with the slope. Consequently, the crest front steepness and the vertical asymmetry factor increase. Overall, the degree of asymmetry of solitary wave profile at breaking increases as the offshore wave height decreases.

- In accordance with previous findings, the relative distance between the cylinder and the breaking point plays a prominent role in obtaining the maximum force. The impact duration and rise time increases as the distance between the cylinder and the breaking point increases. The maximum total force occurs when the wave hits the cylinder just before breaking. The wave height and the rise time during the impact are almost equivalent to the one at the breaking.

- As smaller solitary waves undergo more deformation over a slope before they break, the force contribution from the deformed wave above the still water level to the total force becomes larger. In addition, the forces on the cylinder rise slowly with longer duration, resulting in larger force impulses. It is found that the average slamming coefficient decreases as the incident wave height increases.

Acknowledgement

The authors wish to thank Prof. Atle Jansen and Prof. Phillip L.-F.Liu for providing the experimental data. The research for this paper was supported by the Norwegian Research Center for Offshore Wind Technology (NOWITECH), Research council of Norway (Contract no.193823). The authors also wish to thank NOTUR (Project no. NN9240K) for the allocation of computational resources provided on the Vilje system at the super computing facilities at NTNU.

References

Adeyemo, M. (1968), Effect of beach slope and shoaling on wave asymmetry, *in* 'Proceedings of the 11-th Conference on Coastal Engineering', pp. 145–172.

Alagan Chella, M., Bihs, H. and Myrhaug, D. (2015b), 'Characteristics and profile asymmetry properties of waves breaking over an impermeable submerged reef', *Coast. Eng.* **100**, 26–36.

Alagan Chella, M., Bihs, H., Myrhaug, D. and Muskulus, M. (2015a), 'Breaking characteristics and geometric properties of spilling breakers over slopes', *Coast. Eng.* **95**, 4–19.

Alagan Chella, M., Tørum, A. and Myrhaug, D. (2012), 'An overview of wave impact forces on offshore wind turbine substructures', *Energy Procedia* **20**, 217–226.

Arntsen, Ø. A., Ros, X. and Tørum, A. (2011), Impact forces on a vertical pile from plunging breaking waves, *in* 'Proceedings of the 24-th Conference on Coastal structures'.

Bihs, H., Kamath, A., Alagan Chella, M. and Arntsen, Ø. A. (2016), 'Breaking wave interaction with tandem cylinders under different impact scenarios', *J. Waterw. Port Coast. Ocean Eng.* . DOI: 10.1061/(ASCE)WW.1943-5460.0000343.

Camfield, F. and Street, R. (1979), 'Shoaling of solitary waves on small slopes', *Journal of the Waterway Port Coastal and Ocean Division* **95**, 1–22.

Chakrabarti, S. K., Kriebel, D. and Berek, E. (1997), 'Forces on a single pile caisson in breaking waves and current', *Appl Ocean Res* **19**, 113–140.

Chaplin, J.and Flintham, T., Greated, C. and Skyner, D. (1992), Breaking wave forces on a vertical cylinder, Technical report, Health and Safety Executive, London, UK.

Choi, S., Lee, K. and Gudmestad, O. (2015), 'The effect of dynamic amplification due to a structures vibration on breaking wave impact', *Ocean Eng.* **96**, 8–20.

Chorin, A. (1968), 'Numerical solution of the Navier-Stokes equations', *Math. Comput.* **22**, 745–762.

Cooker, M. J. and Peregrine, D. H. (1990), A model for breaking wave impact pressures, *in* 'Proceedings of the 22nd Conference on Coastal Engineering', pp. 1473–1486.

Cooker, M. J. and Peregrine, D. H. (1995), 'Pressure-impulse theory for liquid impact problems', *J. Fluid Mech.* **297**, 193–214.

Cuomo, G., , Piscopia, R. and Allsop, W. (2011), 'Evaluation of wave impact loads on caisson breakwaters based on joint probability of impact maxima and rise times', *Coast. Eng.* **58**, 9–27.

Cuomo, G., , Tirindelli, M. and Allsop, W. (2007), 'Breaking wave loads at vertical seawalls and breakwaters', *Coast. Eng.* **54**, 657–679.

Cuomo, G., Allsop, W., Bruce, T. and Pearson, J. (2010), 'Breaking wave loads at vertical seawalls and breakwaters', *Coast. Eng.* **57**, 424–439.

Fenton, J. (1985), 'A fifth-order stokes theory for steady waves', *J. Waterw. Port Coast. Ocean Eng.* **111**(2), 216–234.

Galvin, C. J. (1968), 'Breaker type classification on three laboratory beaches', *J. Geophys. Res.* **73**(12), 3651–3659.

Goda, Y., Haranaka, S. and Kitahata, M. (1966), Study of impulsive breaking wave forces on piles, Technical report, Port and Harbor Research Institute, Ministry of Transport.

Goring, D. G. (1978), Tsunamis–the propagation of long waves onto a shelf, PhD thesis, California Institute of Technology.

Grilli, S. T., Subramanya, R., Svendsen, I. A. and Veeramony, J. (1995), 'Shoaling of solitary waves on plane beaches', *J. Waterw. Port Coast. Ocean Eng.* **120**(6), 609–628.

Grilli, S. T., Svendsen, I. A. and Subramanya, R. (1997), 'Breaking criterion and characteristics for solitary waves on slopes', *J. Waterw. Port Coast. Ocean Eng.* **123**(3), 102–112.

Grimshaw, R. (1971), 'The solitary wave in water of variable depth. Part 2.', *J. Fluid Mech.* **46**, 611–622.

Hattori, M., Arami, A. and Yui, T. (1994), 'Wave impact pressure on vertical walls under breaking waves of various types', *Coast. Eng.* **22**, 79–114.

Hieu, P. D., Katsutoshi, T. and Ca, V. T. (2004), 'Numerical simulation of breaking waves using a two-phase flow model', *Appl. Math. Model.* **28**(11), 983–1005.

Hwang, P. A. (1984), Profile asymmetry of shoaling waves on a mild slope, *in* 'Proceedings of the 19-th Conference on Coastal Engineering', pp. 1016–1027.

Ippen, A. T. and Kulin, G. (1954), The shoaling and breaking of the solitary wave, *in* 'Proceedings of the 5-th Conference on Coastal Engineering', pp. 27–47.

Irschik, K., Sparboom, U. and Oumeraci, H. (2002), Breaking wave characteristics for the loading of a slender pile, *in* 'Proceedings of the 28-th Conference on Coastal Engineering', pp. 1341–1352.

Jacobsen, N. G., Fuhrman, D. R. and Fredsøe, J. (2012), 'A wave generation toolbox for the open-source CFD library : OpenFoam', *Int. J. Numer. Methods Fluids* **70**(November), 1073–1088.

Jiang, G. S. and Shu, C. W. (1996), 'Efficient implementation of weighted ENO schemes', *J. Comput. Phys.* **126**, 202–228.

Kamath, A., Alagan Chella, M., Bihs, H. and Arntsen, Ø. A. (2015), 'CFD investigations of wave interaction with a pair of large tandem cylinders', *Ocean Eng.* **108**, 734–748.

Kamath, A., Bihs, H., Alagan Chella, M. and Arntsen, Ø. A. (2016), 'Upstream-cylinder and downstream-cylinder influence on the hydrodynamics of a four-cylinder group', *J. Waterw. Port Coast. Ocean Eng.* . DOI: 10.1061/(ASCE)WW.1943-5460.0000339.

Kjeldsen, S. P. and Myrhaug, D. (1978), Kinematics and dynamics of breaking waves, Technical report, River and Harbour Laboratory (NHL), The Norwegian Institute of Technology.

Kortenhaus, A., Oumeraci, H., Allsop, N., McConnell, K., Van Gelder, P., Hewson, P., Walkden, M., Müller, G., Calabrese, M. and Vicinanza, D. (1999), Wave impact loads-pressures and forces, *in* 'Final Proceedings, MAST III, PROVERBS-Project: Vol. IIa: Hydrodynamic Aspects'.

Larsen, J. and Dancy, H. (1983), 'Open boundaries in short wave simulations - a new approach', *Coast. Eng.* **7**, 285–297.

Lemos, C. M. (1992), 'A simple numerical technique for turbulent flows with free surfaces', *Int. J. Numer. Methods Fluids* **15**, 127–146.

Lin, P. and Liu, P. L.-F. (1998), 'A numerical study of breaking waves in the surf zone', *J. Fluid Mech.* **359**, 239–264.

Losada, M. A., Vidal, C. and Medina, R. (1989), 'Experimental study of the evolution of a solitary wave at an abrupt junction', *J. Geophys. Res.* **94**, 14557–14566.

Miles, J. W. (1980), 'Solitary waves', *Annu. Rev. Fluid Mech.* (12), 11–43.

Mo, W., Jensen, A. and Liu, P. L.-F. (2013), 'Plunging solitary wave and its interaction with a slender cylinder on a sloping beach', *Ocean Eng.* **74**, 48–60.

Munk, W. H. (1949), 'The solitary wave theory and its application to surf problems', *Annals of the New York Academy of Sciences* **3**, 376–424.

Osher, S. and Sethian, J. A. (1988), 'Fronts propagating with curvature-dependent Speed: Algorithms based on Hamilton-Jacobi formulations', *J. Comput. Phys.* **79**, 12–49.

Peregrine, D. H. (2003), 'Water-wave impact on walls', *Annu. Rev. Fluid Mech.* **35**, 23–43.

Sarpkaya, T. and Isaacson, M. (1981), *Mechanics of Wave Forces on Offshore Structures*, Van Nostrand Reinhold Company.

Sawaragi, T. and Nochino, M. (1984), 'Impact forces of nearly breaking waves on a vertical circular cylinder', *Coastal Engineering Journal* **27**, 249–263.

Shu, C. W. and Osher, S. (1988), 'Efficient implementation of essentially non-oscillatory shock capturing schemes', *J. Comput. Phys.* **77**, 439–471.

Stive, M. and Wind, H. (1982), 'A study of radiation stress and set-up in the nearshore region', *Coast. Eng.* **6**, 1–26.

Ting, F. C. K. and Kirby, J. T. (1994), 'Observation of undertow and turbulence in a laboratory surf zone', *Coast. Eng.* **24**(1-2), 51–80.

van der Vorst H. (1992), 'Bi-CGSTAB: A fast and smoothly converging variant of Bi-CG for the solution of nonsymmetric linear systems', *SIAM Journal on scientific and Statistical Computing* **13**, 631–644.

Wienke, J. and Oumeraci, H. (2005), 'Breaking wave impact force on a vertical and inclined slender pile-theoretical and large-scale model investigations', *Coast. Eng.* **52**, 435–416.

Wienke, J., Sparboom, U. and Oumeraci, H. (2000), Breaking wave impact on a slender cylinder, *in* 'Proceedings of the 27th Conference on Coastal Engineering', pp. 1787–1798.

Xiao, H. and Huang, W. (2014), 'Three-dimensional numerical modeling of solitary wave breaking and force on a cylinder pile in a coastal surf zone', *J. Eng. Mech. - ASCE* **141(8)**.

Xie, Z. (2013), 'Two-phase flow modelling of spilling and plunging breaking waves', *Appl. Math. Model.* **37**, 3698–3713.

Zhao, Q., Armfield, S. and Tanimoto, K. (2004), 'Numerical simulation of breaking waves by a multi-scale turbulence model', *Coast. Eng.* **51**(1), 53–80.